ARTICLE IN PRESS

Progress in Particle and Nuclear Physics xxx (xxxx) xxx

Contents lists available at ScienceDirect

Progress in Particle and Nuclear Physics

journal homepage: www.elsevier.com/locate/ppnp

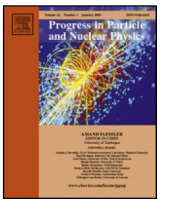

Review

Photoproduction reactions and non-strange baryon spectroscopy

David G. Ireland [a], Eugene Pasyuk [b,*], Igor Strakovsky [c]

[a] SUPA, School of Physics and Astronomy, University of Glasgow, G12 8QQ, UK
[b] Thomas Jefferson National Accelerator Facility, Newport News, VA 23606, USA
[c] The George Washington University, WA, DC 20052, USA

ARTICLE INFO

Article history:
Available online xxxx

Keywords:
Photoproduction
Meson
Nucleon resonance
Baryon spectroscopy

ABSTRACT

We review the last two decades of using photon beams to measure the production of mesons, and in particular the information that can be obtained on the spectrum of light, non-strange baryons. This is a compendium of experimental results, which should be used as a complement to theoretical reviews of the subject. Lists of data sets are given, together with a comprehensive set of references. An indication of the impact of the data is presented with a summary of the results.

Contents

* Corresponding author.
E-mail address: pasyuk@jlab.org (E. Pasyuk).

https://doi.org/10.1016/j.ppnp.2019.103752

Please cite this article as: D.G. Ireland, E. Pasyuk and I. Strakovsky, Photoproduction reactions and non-strange baryon spectroscopy, Progress in Particle and Nuclear Physics (2019) 103752, https://doi.org/10.1016/j.ppnp.2019.103752.

1. Introduction

Measurements of pion photoproduction on both proton and quasi-free neutron targets have a very long history, starting about 70 years ago with the discovery of the pion by the University of Bristol group [1]. Two years later, at the 1949 Spring Meeting of the National Academy of Sciences, a preliminary account was given of some observations of mesons produced by the 335-MeV photon beam from the Berkeley synchrotron [2]. Starting with the use of bremsstrahlung facilities, pioneering results for $\gamma p \to \pi^0 p$ [3–7], $\gamma p \to \pi^+ n$ [8–11], and $\gamma n \to \pi^- p$ [12] were obtained. Despite all the shortcomings of the first measurements (such as large normalization uncertainties, wide energy and angular binning, limited angular coverage and so on), these data were crucial for the discovery of the first excited nucleon state, the $\Delta(1232)3/2^+$, [13].

Whilst the ability of photoproduction measurements to deliver information on baryon resonances had been shown from an early stage, most of the light baryon spectrum states and their properties were subsequently obtained by pion–nucleon scattering. Until the end of the 1970s, meson photoproduction was essentially only able to confirm pion scattering data, without adding a substantial amount of additional information. Indeed, the evolution of particle physics towards energies beyond the regime in which hadronic states are the relevant degree of freedom suggested to some that the study of the light baryon spectrum had come to an end, if not a conclusion. This was summarized in a 1983 review article "Baryon Spectroscopy" by Hey and Kelly [14] who stated in their introduction:

> "Baryon spectroscopy is now thirty years old and perhaps approaching a mid-life crisis. For it is inevitable in such a fast-moving field as high energy particle physics, that experiments have moved on beyond the resonance region to higher energies and different priorities. Thus it is probably no exaggeration to say that we now have essentially *all* the experimental data relevant to the low-energy baryon spectrum, that we are *ever* likely to obtain".

Armed with the benefit of hindsight, and with reference to Fig. 1, we beg to differ! As can be seen in Fig. 1 (Left), most of the data for the pion–nucleon scattering were obtained before the date of the Hey and Kelly review. On the other hand, the 1980s saw several advances in accelerator technology that enabled the production of photon beams of the order of a GeV in energy, whose energy could be accurately enough determined through the tagging of degraded electrons in bremsstrahlung, or via laser backscattering from electron beams. These facilities initially concentrated on photonuclear research, but as soon as the threshold for pion production was reached, it became clear that photon beams for hadron physics research was a reality.

Nevertheless, it took a while for this potential to be realized, which is clearly demonstrated in Fig. 1 (Right). This plot shows that a major increase in the worldwide data set for photoproduction reactions only occurred after the turn of the 21st century. One can readily see that by the time of the Hey and Kelly review [14] (1983), the amount of new data being obtained (both pion- and photoproduction) was indeed tailing off, so their pessimism about more data was at the time well-founded. The beginning of the exponential rise in the number of photoproduction data points around 1996 therefore serves as a starting point for this current review.

The plot does not indicate the relative improvement in the accuracy of the data, which can only be appreciated by delving into the relevant literature. Where initial measurements showed rough energy and angular dependencies, more recent results have been obtained that allow energy scans and fits to angular distributions that allow sophisticated partial wave analyses (PWA), which were previously only possible with pion scattering data.

The scope of this review may seem to be somewhat narrow (a particular set of reactions and only the lightest sector of the baryon spectrum). However, we have limited ourselves to this scope not only to avoid an enormous task of covering all of baryon spectroscopy, but to point out that our knowledge of the light baryon spectrum is not yet complete and that there is a vigorous amount of activity devoted to extracting as much information as possible from the most recent, precise and statistically accurate measurements. In addition, measurements of photoproduction reactions, and in particular those

Please cite this article as: D.G. Ireland, E. Pasyuk and I. Strakovsky, Photoproduction reactions and non-strange baryon spectroscopy, Progress in Particle and Nuclear Physics (2019) 103752, https://doi.org/10.1016/j.ppnp.2019.103752.

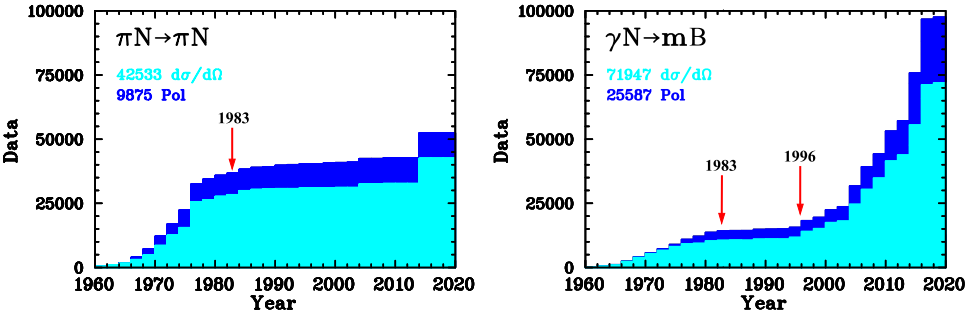

Fig. 1. *Left*: Stacked histogram of the full experimental pion–nucleon scattering database including $\pi^{\pm}p \to \pi^{\pm}p$ and $\pi^{-}p \to \pi^{0}n$. *Right*: Stacked histogram of the full database for single meson photoproduction $\gamma N \to mB$. m = (π, η, η', K, ω), B = (n, p, Λ, Σ). Light shaded – cross sections, dark shaded – polarization data. The experimental data is from the SAID database [15].

on pseudoscalar meson photoproduction including polarization have now been carried out. It is therefore timely to review this work.

In this review, we concentrate on the measurements of physical quantities, and the information that can be extracted from them. We are less concerned with theoretical interpretations other than the identification of new resonances, and leave a discussion of different models to other excellent reviews (e.g., Ref. [16–20]). In this sense, we are taking a *phenomenological* point of view, but our aim is to tie together the many different experimental results over the last couple of decades, and present this unified overview as a starting point for further serious assaults on the understanding of the light baryon spectrum from first principles.

We start with an overview of formalism for dealing with measured data in Section 2, followed in Section 3 by a description of how information can be extracted from the data. In Section 4, we review various experimental facilities that have been used to obtain the data sets, which are described and sorted by final state in Section 5. Some concluding remarks are given in Section 6.

2. Formalism for photoproduction reactions

Experiments only ever measure counts. For a specific beam intensity, hitting a target with a specific density of scattering centers in a specific state of polarization reacting to give a specific final state, whose particles have specific spin orientations, all that an experiment will do is to register counts. The registered counts are subject to the efficiency of the detection apparatus, both in sensitivity and in correctly identifying the desired combination of particles. Advances in experimental technologies are aimed at improving this efficiency so that more complicated measurements can be performed. In the last couple of decades there have been many such advances that have been relevant to photoproduction reactions, including: control and polarization of photon beams, development of polarized gas and solid targets, construction of large solid angle detectors, development of higher rate data acquisition systems and of data analysis and statistical techniques.

What is recorded by an experiment is most likely a distribution of counts in the space of independent kinematic variables, which includes the effect of potentially complicated resolution effects due to the detection apparatus. The data analysis process tries to minimize the resolution effects and to quantify the associated uncertainties (systematic uncertainties). The processed data are then used to estimate physically meaningful quantities, either by binning the counts in one or more dimensions, or by treating the data event-by-event. In any case, there is always uncertainty associated with a finite number of counts (statistical uncertainties).

What are commonly referred to as *observables* are usually theoretical constructs of physically meaningful quantities, and are derived from a consideration of the contributing quantum mechanical amplitudes. Being able to extract information at the amplitude level is therefore seen as a goal of these campaigns, since no more information is available to us, even in principle. Since amplitudes are complex functions, there is always an unknown phase.

A number of amplitude schemes are commonly employed, and the concept of combining observables to realize a *complete* experiment has arisen over the years, which would allow the extraction of all relevant amplitudes up to an unknowable phase. However, given that the observables themselves are related to distributions of measured counts, it is worth stressing that the concept of a complete experiment is only mathematically meaningful.

In practical terms, one does not "observe" observables. One measures counts, either as total intensities or as asymmetries for experimental configurations that can be constructed with combinations of polarized beam, target and recoils. The extensive work done to study the theoretically complete experiment [21–23] can perhaps best be utilized by combining it with an approach to quantify the information content of polarization measurements [24], as a guide to developing the most informative measurements.

In this section we describe both the formalism and how to extract estimates of observables from measurements. We then indicate how this information can be utilized to gain insight into the light baryon resonance spectrum. We

concentrate on single pseudoscalar meson photoproduction, since it is the most straightforward reaction in terms of measurement and formalism, to give a flavor of the relevant issues. Double pseudoscalar meson and vector meson photoproduction require more complicated formalisms, and we will refer the reader to the relevant literature in the interests of saving space.

2.1. Amplitudes and observables

2.1.1. Single pseudoscalar meson photoproduction

Single pseudoscalar meson photoproduction involves the interaction of a photon with a free proton, a bound neutron or a whole nucleus. For studies of the baryon spectrum, we are normally interested in the first two of these. So a spin-1 particle (the photon, two helicity states) and a spin-$\frac{1}{2}$ particle (the nucleon) react to give a spin-0 particle (the pseudoscalar meson) and a spin-$\frac{1}{2}$ particle (the recoiling baryon). This gives eight spin combinations, of which four are possible within the parity-conserving strong interaction that has taken place. The four combinations are represented as amplitudes, the exact form of which is a matter of choice. Common options are CGLN [25], helicity amplitudes [26] and transversity amplitudes [21]. Within any of these bases, there are 16 possible bilinear combinations that are referred to as the "observables".

To illustrate this in detail, a completely general expression for the cross section of these reactions following Ref. [27], with the explicit dependence on the observables, is given below:

$$
\begin{aligned}
\mathbf{d}\sigma^{\mathbf{B,T,R}}(\vec{P^{\gamma}},\vec{P^{T}},\vec{P^{R}},\phi) \quad &= \quad \frac{1}{2}\left\{\mathbf{d}\sigma_{\mathbf{0}}\left[1-P_L^{\gamma}P_y^{T}P_{y'}^{R}\cos 2(\alpha-\phi)\right]\right. && \text{(1a)}\\
\text{Single spin observables} \quad &+\boldsymbol{\Sigma}\left[-P_L^{\gamma}\cos 2(\alpha-\phi)+P_y^{T}P_{y'}^{R}\right] && \text{(1b)}\\
&+\mathbf{T}\left[P_y^{T}-P_L^{\gamma}P_{y'}^{R}\cos 2(\alpha-\phi)\right] && \text{(1c)}\\
&+\mathbf{P}\left[P_{y'}^{R}-P_L^{\gamma}P_y^{T}\cos 2(\alpha-\phi)\right] && \text{(1d)}\\
\text{Beam–Target observables} \quad &+\mathbf{E}\left[-P_{\odot}^{\gamma}P_z^{T}+P_L^{\gamma}P_x^{T}P_{y'}^{R}\sin 2(\alpha-\phi)\right] && \text{(1e)}\\
&+\mathbf{G}\left[P_L^{\gamma}P_z^{T}\sin 2(\alpha-\phi)+P_{\odot}^{\gamma}P_x^{T}P_{y'}^{R}\right] && \text{(1f)}\\
&+\mathbf{F}\left[P_{\odot}^{\gamma}P_x^{T}+P_L^{\gamma}P_z^{T}P_{y'}^{R}\sin 2(\alpha-\phi)\right] && \text{(1g)}\\
&+\mathbf{H}\left[P_L^{\gamma}P_x^{T}\sin 2(\alpha-\phi)-P_{\odot}^{\gamma}P_x^{T}P_{y'}^{R}\right] && \text{(1h)}\\
\text{Beam–Recoil observables} \quad &+\mathbf{C_{x'}}\left[P_{\odot}^{\gamma}P_{x'}^{R}-P_L^{\gamma}P_y^{T}P_{z'}^{R}\sin 2(\alpha-\phi)\right] && \text{(1i)}\\
&+\mathbf{C_{z'}}\left[P_{\odot}^{\gamma}P_{z'}^{R}-P_L^{\gamma}P_y^{T}P_{x'}^{R}\sin 2(\alpha-\phi)\right] && \text{(1j)}\\
&+\mathbf{O_{x'}}\left[P_L^{\gamma}P_{x'}^{R}\sin 2(\alpha-\phi)+P_{\odot}^{\gamma}P_y^{T}P_{z'}^{R}\right] && \text{(1k)}\\
&+\mathbf{O_{z'}}\left[P_L^{\gamma}P_{z'}^{R}\sin 2(\alpha-\phi)-P_{\odot}^{\gamma}P_y^{T}P_{x'}^{R}\right] && \text{(1l)}\\
\text{Target–Recoil observables} \quad &+\mathbf{L_{x'}}\left[P_z^{T}P_{x'}^{R}+P_L^{\gamma}P_x^{T}P_{z'}^{R}\cos 2(\alpha-\phi)\right] && \text{(1m)}\\
&+\mathbf{L_{z'}}\left[P_z^{T}P_{z'}^{R}-P_L^{\gamma}P_x^{T}P_{x'}^{R}\cos 2(\alpha-\phi)\right] && \text{(1n)}\\
&+\mathbf{T_{x'}}\left[P_x^{T}P_{x'}^{R}+P_L^{\gamma}P_z^{T}P_{z'}^{R}\cos 2(\alpha-\phi)\right] && \text{(1o)}\\
&\left.+\mathbf{T_{z'}}\left[P_x^{T}P_{z'}^{R}-P_L^{\gamma}P_z^{T}P_{x'}^{R}\cos 2(\alpha-\phi)\right]\right\} && \text{(1p)}
\end{aligned}
$$

In these equations, σ_0 denotes unpolarized cross section, P_L^{γ} denotes degree of linear photon polarization, $P_{\odot}^{\gamma}$ denotes degree of circular photon polarization, $P_{x,y,z}^{T}$ and $P_{x',y',z'}^{R}$ describe target and recoil baryon polarization components. The angle ϕ is the azimuthal angle of the reaction plane, which is defined in the diagram in Fig. 2.

$\boldsymbol{\Sigma}$, **T**, and **P** are the single beam, target and recoil spin asymmetries. **E**, **G**, **H** and **F** are the beam–target double spin asymmetries; $\mathbf{C_{x'}}$, $\mathbf{C_{z'}}$, $\mathbf{O_{x'}}$ and $\mathbf{O_{z'}}$ are the beam–recoil double spin asymmetries; $\mathbf{T_{x'}}$, $\mathbf{T_{z'}}$, $\mathbf{L_{x'}}$, and $\mathbf{L_{z'}}$ are the target–recoil double spin asymmetries. The primes refer to a coordinate system in which $\hat{z'}$ is parallel to the pseudoscalar meson momentum, $\hat{y'}$ is normal to the scattering plane and $\hat{x'} = \hat{y'} \times \hat{z'}$. The unprimed coordinate system has $\hat{z}$ parallel the photon momentum, $\hat{y}$ is normal to the scattering plane and $\hat{x} = \hat{y} \times \hat{z}$.

In Eqs. (1a) to (1p), it can be seen that each observable enters twice. This means that there are always experimental configurations that can be used to extract the values, some of which require triple polarization measurements. Whilst not strictly required, the extraction of observables from two experimental configurations is desirable in order to reduce systematic uncertainties.

2.1.2. Two pseudoscalar meson photoproduction

Reactions such as $\gamma p \rightarrow p\pi^+\pi^-$, as well as any other two pseudoscalar mesons reactions, have three body final states and therefore have more independent kinematic variables and observables. Fig. 3 illustrates the momenta involved. Formalism relating amplitudes and observables for these reactions is discussed detail in Ref. [28]. Writing a full cross

Please cite this article as: D.G. Ireland, E. Pasyuk and I. Strakovsky, Photoproduction reactions and non-strange baryon spectroscopy, Progress in Particle and Nuclear Physics (2019) 103752, https://doi.org/10.1016/j.ppnp.2019.103752.

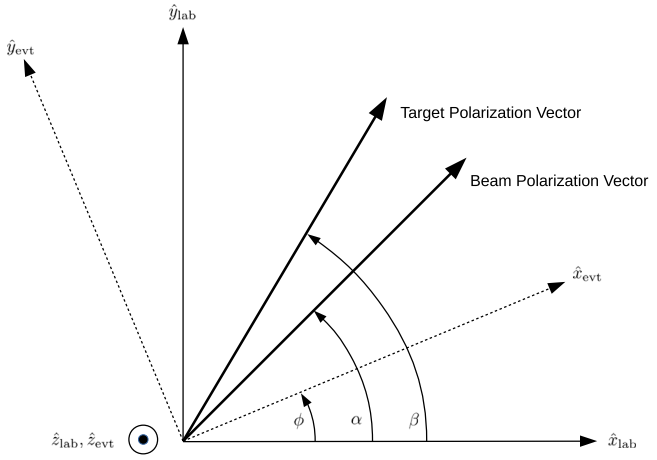

Fig. 2. The definitions of laboratory and event axes, as well as azimuthal angles. The common laboratory, center-of-mass and event z-axis is directed out of the page. The lab x- and y-axes are in the horizontal and vertical directions, and the event y-axis is normal to the reaction plane.

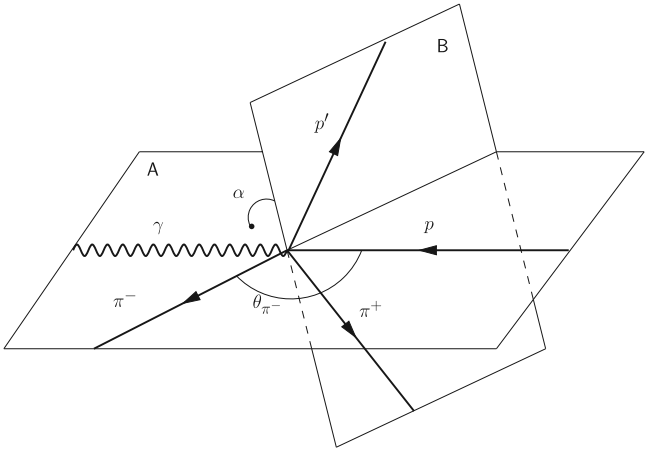

Fig. 3. Angular kinematic variables for the reaction $\gamma p \to \pi^+\pi^- p'$ in the CM frame. The set with $i = \pi^-$, $j = \pi^+$, and $k = p'$ includes the angular variables for θ_{π^-}, the polar angle of the π^-, and $\alpha[\pi^- p][\pi^+ p']$, which is the angle between the planes A and B, where plane A ($[\pi^- p]$) is defined by the 3-momenta of the π^- and the initial state proton and plane B ($[\pi^+ p']$) is defined by the 3-momenta of the π^+ and the final state proton p'. The polar angle $\theta_{p'}$ is relevant for the set with $i = p'$, $j = \pi^+$, and $k = \pi^-$, while the polar angle θ_{π^-} belongs to the set with $i = \pi^+$, $j = p'$, and $k = \pi^-$.

section formula in component form is not practical, so we illustrate a more special case with a vector notation. In case of polarized photons and polarized target, using notation consistent with the previous section, the cross section can be written as:

$$\begin{aligned}\mathbf{d}\sigma^{\mathbf{B},\mathbf{T}}(\vec{P^\gamma}, \vec{P^T}, x_i) = \mathbf{d}\sigma_\mathbf{0}\{&(1 + \vec{P^T}\cdot\vec{\mathbf{P}}) \\ &+ P^\gamma_\odot(\mathbf{I}^\odot + \vec{P^T}\cdot\vec{\mathbf{P}}^\odot) \\ &+ P^\gamma_L[\sin 2(\alpha-\phi)(\mathbf{I}^\mathbf{s} + \vec{P^T}\cdot\vec{\mathbf{P}}^\mathbf{s}) \\ &+ \cos 2(\alpha-\phi)(\mathbf{I}^\mathbf{c} + \vec{P^T}\cdot\vec{\mathbf{P}}^\mathbf{c})],\}\end{aligned} \tag{2}$$

where:
$\mathbf{d}\sigma_\mathbf{0}$ is the unpolarized cross section;
$\alpha - \phi$ is the angle between photon polarization and reaction plane;
x_i represents all the kinematic variables;
$P^\gamma_\odot$, P^γ_L are the degrees of circular or linear photon polarization;
$\vec{P^T}$ is the target nucleon polarization (P^T_x, P^T_y, P^T_z);
The observables in this case are:
$\mathbf{I}^{\odot,\mathbf{s},\mathbf{c}}$ single spin beam asymmetries associated with polarized photons;

$\vec{\mathbf{P}}$ target asymmetry ($\mathbf{P_x}$, $\mathbf{P_y}$, $\mathbf{P_z}$);
$\vec{\mathbf{P}}^{\odot,\mathbf{s,c}}$ double spin asymmetries ($\mathbf{P}_\mathbf{x}^\odot$, $\mathbf{P}_\mathbf{y}^\odot$, $\mathbf{P}_\mathbf{z}^\odot$), ($\mathbf{P}_\mathbf{x}^\mathbf{s}$, $\mathbf{P}_\mathbf{y}^\mathbf{s}$, $\mathbf{P}_\mathbf{z}^\mathbf{s}$), ($\mathbf{P}_\mathbf{x}^\mathbf{c}$, $\mathbf{P}_\mathbf{y}^\mathbf{c}$, $\mathbf{P}_\mathbf{z}^\mathbf{c}$).
In these reactions there are a total of 64 possible observables. In practice, however, it would be extremely challenging to extract all of these with reasonable accuracy, so published experiments tend to concentrate on a few of them.

2.1.3. Vector meson photoproduction

With a spin-1 vector meson in the final state, the number of underlying helicity amplitudes is 12, which would require a total of 23 independent observables at each energy and angle to extract. As with the full suite of two-pion spin observables, it may never be practical to extract all of them.

The decay angular distributions of the vector mesons can be examined to extract some of the spin density matrix elements (SDMEs). A comprehensive guide to this formalism is given in Ref. [29]. The SDMEs are defined in the rest frame of the vector meson, however the effects of resonances and other mechanisms relevant to the low energy baryon spectrum require that spin observables be measured in the γN center of mass frame [30].

In this review, we restrict ourselves to ω photoproduction; ρ photoproduction is predominantly analyzed in the context of two pion photoproduction, and other light vector mesons such as the $\phi(1020)$ and $K^*(892)$ have hitherto had limited impact on studies of the light baryon spectrum.

3. How to extract observables and amplitudes from the data

The number of counts N registered in a detector of efficiency ε, subtending solid angle $d\Omega$, at a center-of-mass energy E and in a measurement of luminosity $\mathcal{L}$ for a total time T, is given by

$$N(\theta,\phi,E) = \int_0^T \mathcal{L}(E)dt \int \frac{1}{\varepsilon(\theta,\phi,E)} \frac{d\sigma(\theta,\phi,E)}{d\Omega} d\Omega, \tag{3}$$

where the *efficiency* is the ratio of the number of particles of interest identified by the detector to the number of the particles passing through the solid angle at an energy E, the *luminosity* is a (possibly time-dependent) product of beam flux and density of scattering centers. The process also depends on beam energy. To simplify notation we write that for a specific experimental configuration i,

$$N_i = \varepsilon_i^{-1}\mathcal{L}_i\sigma_i, \tag{4}$$

where it is implicit that $\mathcal{L}_i$ is an integrated luminosity for the configuration, and that σ_i is the differential cross section, which could depend on energy and scattering angles.[1]

The efficiency and the luminosity are experiment-dependent, whereas the cross section contains all the physics information and is a link to theoretical models of the reaction.

The main observable for any reaction of interest is the cross section, and its determination as a function of energy and angle requires careful setup and handling of the beam, target and detector systems, in order to obtain an accurate value for the luminosity and efficiency of the experiment. If the experiment is set up so that the spin configuration of beam, target or recoils is not fixed then the cross section represents a sum over initial spins and an average over final spins. If the experiment does contain an element of polarization, then the distribution of cross section will contain additional dependence on the kinematics of the reaction and the degrees of polarization. Since theoretical models of cross sections are calculated from coherent sums of amplitudes that are dependent on the individual spin combinations of beam, target and recoiling products, it is desirable to evaluate these as well.

Table 1 summarizes the distributions for the various experimental configurations, where we again limit the discussion to single pseudoscalar meson photoproduction. The main point of this table is to illustrate that as more elements of the experimental configuration are polarized, the more complicated is the dependence of the intensity distribution on the number of observables.

Rather than measuring cross-sections for specific polarization configurations, a common technique is to access them by measuring *asymmetries*. Defining in general the notation for asymmetry in the number of counts between two experimental configurations i and j

$$A_N = \frac{N_i - N_j}{N_i + N_j} = \frac{\varepsilon_i^{-1}\mathcal{L}_i\sigma_i - \varepsilon_j^{-1}\mathcal{L}_j\sigma_j}{\varepsilon_i^{-1}\mathcal{L}_i\sigma_i + \varepsilon_j^{-1}\mathcal{L}_j\sigma_j}, \tag{6}$$

and introducing the further notation

$$A_\mathcal{L} = \frac{\mathcal{L}_i - \mathcal{L}_j}{\mathcal{L}_i + \mathcal{L}_j}; \qquad A_\varepsilon = \frac{\varepsilon_i - \varepsilon_j}{\varepsilon_i + \varepsilon_j}; \qquad A_\sigma = \frac{\sigma_i - \sigma_j}{\sigma_i + \sigma_j}; \tag{7}$$

we find

$$A_N = \frac{A_\sigma + A_\mathcal{L} - A_\varepsilon - A_\sigma A_\mathcal{L} A_\varepsilon}{1 - A_\mathcal{L}A_\varepsilon - A_\sigma A_\varepsilon + A_\sigma A_\mathcal{L}}. \tag{8}$$

[1] We will simply refer to these quantities as "luminosity" and "cross section" hereafter.

Table 1
Expressions for cross sections for different experiments.

Configuration			*Cross section formula, σ/σ_0*	
Beam	Target	Recoil		
Unpolarized	Unpolarized	N	1	(5a)
		Y	$1 + \mathbf{P}P^R_{y'}$	(5b)
	Longitudinal	N	1	(5c)
		Y	$1 + \mathbf{P}P^R_{y'} + \left(\mathbf{L_{x'}}P^R_{x'} + \mathbf{L_{z'}}P^R_{z'}\right)P^T_z$	(5d)
	Transverse	N	$1 + \mathbf{T}P^T_T \sin(\beta-\phi)$	(5e)
		Y	$1 + \mathbf{P}P^R_{y'} + \left(\mathbf{\Sigma}P^R_{y'} + \mathbf{T}\right)P^T_T \sin(\beta-\phi)$ $+ \left(\mathbf{T_{x'}}P^R_{x'} + \mathbf{T_{z'}}P^R_{z'}\right)P^T_T \cos(\beta-\phi)$	(5f)
Circular	Unpolarized	N	1	(5g)
		Y	$1 + \mathbf{P}P^R_{y'} + \left(\mathbf{C_{x'}}P^R_{x'} + \mathbf{C_{z'}}P^R_{z'}\right)P^\gamma_\odot$	(5h)
	Longitudinal	N	$1 - \mathbf{E}P^\gamma_\odot P^T_y$	(5i)
		Y	$1 + \mathbf{P}P^R_{y'} + \left(\mathbf{L_{x'}}P^R_{x'} + \mathbf{L_{z'}}P^R_{z'}\right)P^T_z$ $+ \left\{\mathbf{C_{x'}}P^R_{x'} + \mathbf{C_{z'}}P^R_{z'} - \left(\mathbf{E} + \mathbf{H}P^R_{y'}\right)P^T_z\right\}P^\gamma_\odot$	(5j)
	Transverse	N	$1 + \mathbf{T}P^T_T \sin(\beta-\phi) + \mathbf{F}P^\gamma_\odot P^T_T \cos(\beta-\phi)$	(5k)
		Y	$1 + \mathbf{P}P^R_{y'} + \left(\mathbf{\Sigma}P^R_{y'} + \mathbf{T}\right)P^T_T \sin(\beta-\phi)$ $+ \left(\mathbf{T_{x'}}P^R_{x'} + \mathbf{T_{z'}}P^R_{z'}\right)P^T_T \cos(\beta-\phi)$ $+ \left\{\mathbf{C_{x'}}P^R_{x'} + \mathbf{C_{z'}}P^R_{z'} + \left(\mathbf{F} + \mathbf{G}P^R_{y'}\right)P^T_T \cos(\beta-\phi)\right.$ $\left. + \left(\mathbf{O_{x'}}P^R_{z'} - \mathbf{O_{z'}}P^R_{x'}\right)P^T_T \sin(\beta-\phi)\right\}P^\gamma_\odot$	(5l)
Linear	Unpolarized	N	$1 - \mathbf{\Sigma}P^\gamma_L \cos 2(\alpha-\phi)$	(5m)
		Y	$1 + \mathbf{P}P^R_{y'} - \left\{\mathbf{\Sigma} + \mathbf{T}P^R_{y'}\right\}P^\gamma_L \cos 2(\alpha-\phi)$ $+ \left\{\mathbf{O_{x'}}P^R_{x'} + \mathbf{O_{z'}}P^R_{z'}\right\}P^\gamma_L \sin 2(\alpha-\phi)$	(5n)
	Longitudinal	N	$1 - \mathbf{\Sigma}P^\gamma_L \cos 2(\alpha-\phi) + \mathbf{G}P^T_y P^\gamma_L \sin 2(\alpha-\phi)$	(5o)
		Y	$1 + \mathbf{P}P^R_{y'} + \left(\mathbf{L_{x'}}P^R_{x'} + \mathbf{L_{z'}}P^R_{z'}\right)P^T_z$ $- \left\{\mathbf{\Sigma} + \mathbf{T}P^R_{y'} + \left(\mathbf{T_{x'}}P^R_{z'} - \mathbf{T_{z'}}P^R_{x'}\right)P^T_z\right\}P^\gamma_L \cos 2(\alpha-\phi)$ $+ \left\{\left(\mathbf{F}P^R_{y'} + \mathbf{G}\right)P^T_z + \mathbf{O_{x'}}P^R_{x'} + \mathbf{O_{z'}}P^R_{z'}\right\}P^\gamma_L \sin 2(\alpha-\phi)$	(5p)
	Transverse	N	$1 + \mathbf{T}P^T_T \sin(\beta-\phi)$ $- \left\{\mathbf{\Sigma} + \mathbf{P}P^T_T \sin(\beta-\phi)\right\}P^\gamma_L \cos 2(\alpha-\phi)$ $+ \mathbf{H}P^T_T \cos(\beta-\phi)P^\gamma_L \sin 2(\alpha-\phi)$	(5q)
		Y	$1 - P^\gamma_L P^R_{y'} P^T_T \sin(\beta-\phi)\cos 2(\alpha-\phi) + \mathbf{P}P^R_{y'}$ $+ \left(\mathbf{T_{x'}}P^R_{x'} + \mathbf{T_{z'}}P^R_{z'}\right)P^T_T \cos(\beta-\phi)$ $+ \left(\mathbf{\Sigma}P^R_{y'} + \mathbf{T}\right)P^T_T \sin(\beta-\phi)$ $- \left\{\mathbf{\Sigma} + \mathbf{T}P^R_{y'} + \mathbf{P}P^T_T \sin(\beta-\phi)\right.$ $\left. - \left(\mathbf{L_{x'}}P^R_{z'} - \mathbf{L_{z'}}P^R_{x'}\right)P^T_T \cos(\beta-\phi)\right\}P^\gamma_L \cos 2(\alpha-\phi)$ $+ \left\{\mathbf{O_{x'}}P^R_{x'} + \mathbf{O_{z'}}P^R_{z'} + \left(\mathbf{E}P^R_{y'} + \mathbf{H}\right)P^T_T \cos(\beta-\phi)\right.$ $\left. - \left(\mathbf{C_{x'}}P^R_{z'} - \mathbf{C_{z'}}P^R_{x'}\right)P^T_T \sin(\beta-\phi)\right\}P^\gamma_L \sin 2(\alpha-\phi)$	(5r)

In most cases, the difference in efficiency between two settings will be close to, if not identically, zero, and the expression simplifies to

$$A_N = \frac{A_\sigma + A_\mathcal{L}}{1 + A_\sigma A_\mathcal{L}}, \tag{9}$$

which shows that if $A_\mathcal{L}$ can be made small (i.e., the luminosity in the two settings is roughly equal), the main driver in the asymmetry of counts will be in A_σ, which contains the physics quantities of interest.

For a given setting $\mathcal{S}$ of a configuration of beam and target polarization, the cross section formula can be written in a simple form

$$\sigma = u + \mathcal{S}v, \tag{10}$$

where u is a function of everything that does not depend on the setting $\mathcal{S}$ and v is a function of everything that does depend on it. If we have two settings, $\mathcal{S}_i$ and $\mathcal{S}_j$ then

$$A_\sigma = \frac{\left(\mathcal{S}_i - \mathcal{S}_j\right)v}{2u + \left(\mathcal{S}_i + \mathcal{S}_j\right)v}, \tag{11}$$

Please cite this article as: D.G. Ireland, E. Pasyuk and I. Strakovsky, Photoproduction reactions and non-strange baryon spectroscopy, Progress in Particle and Nuclear Physics (2019) 103752, https://doi.org/10.1016/j.ppnp.2019.103752.

Table 2
Expressions for asymmetries for different experiments. The definitions of angles are shown in Fig. 2. Configurations are labeled U, C and L for unpolarized, circular and linear polarized photon beams; U, L and T for unpolarized, longitudinal and transverse target polarization. Where degrees of polarization are labeled +ve or −ve, this refers to their direction with respect to an axis: lab x, y or z for target polarization; photon beam direction for circular photon polarization.

Configuration			*Asymmetry formula, A_σ*	
Beam	Target	Settings		
U	L	P_z^T +ve; P_z^T −ve	$\frac{P_z^T\left(\mathbf{L}_{x'}P_{x'}^R+\mathbf{L}_{z'}P_{z'}^R\right)}{1+\mathbf{P}P_{y'}^R}$	(13a)
	T	$\beta=0;\ \beta=\pi$	$\frac{P_T^T}{1+\mathbf{P}P_{y'}^R}\left\{\left(\mathbf{T}_{x'}P_{x'}^R+\mathbf{T}_{z'}P_{z'}^R\right)\cos\phi - \left(\mathbf{\Sigma}P_{y'}^R+\mathbf{T}\right)\sin\phi\right\}$	(13b)
C	U	$P_\odot^\gamma$ +ve; $P_\odot^\gamma$ −ve	$\frac{P_\odot^\gamma\left(\mathbf{C}_{x'}P_{x'}^R+\mathbf{C}_{z'}P_{z'}^R\right)}{1+\mathbf{P}P_{y'}^R}$	(13c)
	L	$(P_\odot^\gamma$ +ve, P_z^T +ve | $P_\odot^\gamma$ −ve, P_z^T −ve); $(P_\odot^\gamma$ +ve, P_z^T −ve | $P_\odot^\gamma$ −ve, P_z^T +ve)	$\frac{P_\odot^\gamma P_z^T\left(\mathbf{E}+\mathbf{H}P_{y'}^R\right)}{1+\mathbf{P}P_{y'}^R}$	(13d)
	T	$(P_\odot^\gamma$ +ve, $\beta=0$ | $P_\odot^\gamma$ −ve, $\beta=\pi$); $(P_\odot^\gamma$ +ve, $\beta=0$ | $P_\odot^\gamma$ −ve, $\beta=\pi$)	$\frac{P_\odot^\gamma P_T^T}{1+\mathbf{P}P_{y'}^R}\left\{\left(\mathbf{F}+\mathbf{G}P_{y'}^R\right)\cos\phi - \left(\mathbf{O}_{x'}P_{z'}^R-\mathbf{O}_{z'}P_{x'}^R\right)\sin\phi\right\}$	(13e)
L	U	$\alpha=0;\ \alpha=\frac{\pi}{2}$	$\frac{-P_L^\gamma}{1+\mathbf{P}P_{y'}^R}\left\{\left(\mathbf{\Sigma}+\mathbf{T}P_{y'}^R\right)\cos2\phi + \left(\mathbf{O}_{x'}P_{x'}^R-\mathbf{O}_{z'}P_{z'}^R\right)\sin2\phi\right\}$	(13f)
	L	$(\alpha=0, P_z^T$ +ve | $\alpha=\frac{\pi}{2}, P_z^T$ −ve); $(\alpha=0, P_z^T$ −ve | $\alpha=\frac{\pi}{2}, P_z^T$ +ve)	$\frac{-P_L^\gamma P_z^T}{1+\mathbf{P}P_{y'}^R}\left\{\left(\mathbf{T}_{x'}P_{z'}^R-\mathbf{T}_{z'}P_{x'}^R\right)\cos2\phi + \left(\mathbf{F}P_{y'}^R+\mathbf{G}\right)\sin2\phi\right\}$	(13g)
	T	$(\alpha=0, \beta=0$ | $\alpha=\frac{\pi}{2}, \beta=\pi$); $(\alpha=0, \beta=0$ | $\alpha=\frac{\pi}{2}, \beta=\pi$)	$\frac{P_L^\gamma P_T^T}{1+\mathbf{P}P_{y'}^R}\left\{\left(P_{y'}^R+\mathbf{P}\right)\sin\phi\cos2\phi + \left(\mathbf{L}_{x'}P_{z'}^R-\mathbf{L}_{z'}P_{x'}^R\right)\cos\phi\cos2\phi + \left(\mathbf{C}_{x'}P_{z'}^R-\mathbf{C}_{z'}P_{x'}^R\right)\sin\phi\sin2\phi + \left(\mathbf{E}P_{y'}^R+\mathbf{H}\right)\cos\phi\sin2\phi\right\}$	(13h)

so that if we can arrange $\mathcal{S}_j = -\mathcal{S}_i$ this would maximally isolate the function v in the asymmetry. This may not be possible to achieve in practice, so if the best we can do is $\mathcal{S}_j = 2\delta - \mathcal{S}_i$, where δ represents half the difference in *degree* of polarization between the two settings, then

$$A_\sigma = \frac{(s_i+\delta)\,v}{u+\delta v}, \tag{12}$$

where $s_i \in [0, 1]$ is the degree of polarization in setting $\mathcal{S}_i$.

To make this less abstract, we give in Table 2 some examples of A_σs for a range of beam and target polarization settings. For clarity we take $\delta = 0$, so that $A_\sigma = s_i v/u$ but note the straightforward extension to Eq. (12) if the degree of polarization is different between settings. We include the terms related to recoil polarization measurement, which can be removed if recoil polarization is not determined (i.e., set $P_{x'}^R = P_{y'}^R = P_{z'}^R = 0$). Note that in some cases, such as the identification of Λs from the decay to πp by detecting the pion or proton, there will be sensitivity to recoil polarization, so those terms cannot be removed.

Tables 1 and 2 show that in practice observables are always measured in combinations. The final, but most technically challenging measurement, given by Eq. (5r) in Table 1 is perhaps the nearest one could claim to being a "complete experiment" as it is sensitive to a "complete set" of observables, but note that it is additionally sensitive to several more observables. The more important challenge is to perform measurements with sufficient accuracy. A rule of thumb is that pseudoscalar photoproduction observables need to be measured to better than $\pm \sim 0.5$ to provide any information.

Please cite this article as: D.G. Ireland, E. Pasyuk and I. Strakovsky, Photoproduction reactions and non-strange baryon spectroscopy, Progress in Particle and Nuclear Physics (2019) 103752, https://doi.org/10.1016/j.ppnp.2019.103752.

3.1. How to extract parameters of nucleon resonances from the photoproduction data

Very simply put, one constructs a data model whose parameters are explicitly or implicitly related to physical parameters such as masses, branching ratios and coupling constants. The data model can be constructed from a physics model of the reaction. Physics models can vary from simply describing a single reaction channel at the tree level, to complicated coupled-channel models that require the analysis of *any* reaction that can kinematically contribute to a final state. The advantage of a single-channel reaction model is that it is relatively straightforward to calculate and to obtain a rough idea of the main contributions from resonances. The disadvantage of this is that the extracted parameters are more difficult to interpret when comparing results for different channels. A coupled-channels approach on the other hand allows one to extract coupling constants and other parameters in such a way as to be consistent between channels, at the expense of having to estimate sometimes hundreds of parameters, which requires heavy computational resource.

In doing this there are a number of complications. For instance, how does one choose which resonant states to include? This is a model comparison problem, since adding more resonances will mean the addition of more parameters, thereby making a fit to the data easier. On the other hand, an Occam's razor approach to keep the model as simple as possible should act to reduce the number of resonances that require to be invoked.

Alternatively one may want to extract information in a "model independent" way. By analyzing distributions in energy and angle, a partial-wave analysis (PWA) can be carried out in which the intensity and phase of each partial wave can be examined to determine the contributions of different resonances. Again, there is a model comparison issue with the question of how many partial waves to include in fits.

Originally, PWA arose as the technology to determine the amplitudes of a reaction through fitting scattering data. This is a non-trivial mathematical problem — looking for a solution of an ill-posed problem, as described in Hadamard [31] and Tikhonov [32]. Resonances appeared as a by-product (bound states objects with definite quantum numbers, mass, lifetime and so on). Standard PWA reveals resonances that are not too wide ($\Gamma < 500$ MeV) and possess a large enough elastic branching ratio (BR $> 4\%$). It is possible, however, to miss narrow resonances with $\Gamma < 30$ MeV [33].

Whether one wants to extract physics from the data by fitting model parameters or projecting out partial waves, there is a choice as to how to use the data. If the phenomenology group is well enough connected with the experiments, it can be possible to construct likelihood functions on an event-by-event basis. This approach does require high numbers of events for the results to be robust, but means that quantities are not averaged over regions of phase space. A more common interface between experiment and theory is for the experimenters to report the values of observables, which have been binned in energy and angles. At the current levels of accuracy, both approaches are yielding similar results.

3.1.1. Resonance parameters

The main objectives of PWA schemes, apart from establishing the existence of resonances, are to derive estimates of resonance properties such as mass, width, branching ratios, couplings, etc. Calling an object a resonance implies that there is a resonant frequency and an associated width that characterizes the state. By analogy with mechanical resonances Breit–Wigner (BW) parameters, mass and width, can be used to describe each resonance, but their exact values depend on the model-dependent method of extraction. The preferred approach, as described in the Review of Particle Physics [34], is for an analysis to estimate the position of poles in the complex energy plane.

3.2. Reactions on neutron targets

Only with good data on both proton and neutron targets, can one hope to disentangle the isoscalar and isovector electromagnetic couplings of various N^* and Δ^* resonances, as well as the isospin properties of non-resonant background amplitudes [35,36].

Unfortunately, there is no free neutron target. The radiative decay width of neutral baryons may be extracted from π^- and π^0 photoproduction from neutrons, but in practice one can only use a target containing a bound neutron. To extract relevant information one requires the use of model-dependent final-state interaction (FSI) corrections [35,37]. There is no way to isolate FSI experimentally [38,39].

At lower energies (E < 700 MeV), there are data for the inverse π^- photoproduction reaction, $\pi^- p \to \gamma n$. This process is free from complications associated with a deuteron target. However, there is a major disadvantage of using $\pi^- p \to \gamma n$: there is a large background from $\pi^- p \to \pi^0 n \to \gamma\gamma n$ reactions, whose cross section is 5 to 500 times larger than $\pi^- p \to \gamma n$.

Studies of the $\gamma n \to \pi^- p$ and $\gamma n \to \pi^0 n$ reactions can be carried out in quasi-free kinematics with deuteron targets. The reactions $\gamma d \to \pi^- p(p)$ and $\gamma d \to \pi^0 n(p)$ in these kinematics have a fast, knocked-out nucleon and a slow proton spectator, and the slow proton is assumed not to be involved in the pion production process. In this quasi-free region, the reaction mechanism corresponds to the "dominant" impulse approximation (IA) diagram in Fig. 4(a) with the slow proton emerging from the deuteron vertex. Here, the differential cross section on the deuteron can be related to that on the neutron target in a well understood way [38,39]. Fig. 4 illustrates this dominant IA diagram, as well as the leading terms of FSI corrections.

An energy and angle dependent FSI correction factor, $R(E, \theta)$, can be defined as the ratio between the sum of three dominant diagrams in Fig. 4 and IA (the first of the diagrams). This can then be applied to the experimental γd data to get a two-body cross section for $\gamma n \to \pi^- p$ and $\gamma n \to \pi^0 n$.

Please cite this article as: D.G. Ireland, E. Pasyuk and I. Strakovsky, Photoproduction reactions and non-strange baryon spectroscopy, Progress in Particle and Nuclear Physics (2019) 103752, https://doi.org/10.1016/j.ppnp.2019.103752.

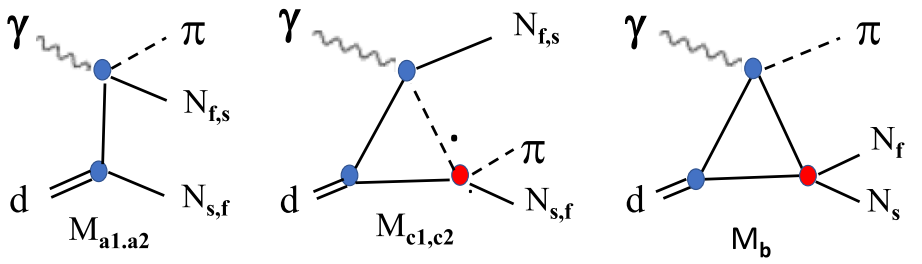

Fig. 4. The IA (M_{a1}, M_{a2}), NN-FSI (M_b), and πN (M_{c1}, M_{c2}) diagrams for the reaction $\gamma d \to \pi N$. Wavy, solid, dashed and double lines correspond to the photon, nucleons, pion, and deuteron, respectively.

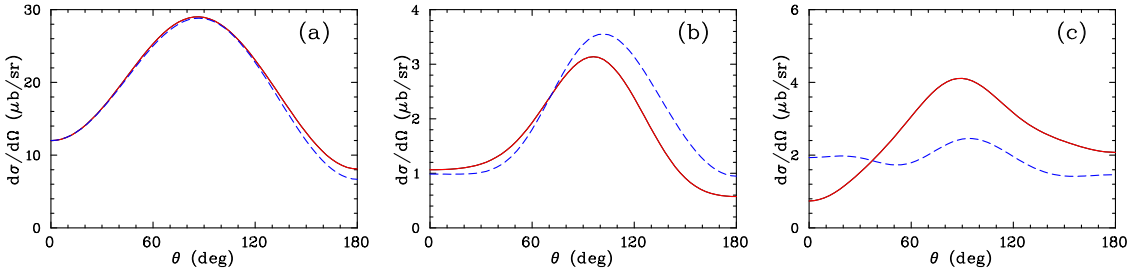

Fig. 5. The differential cross sections of the $\gamma p \to \pi^0 p$ (red solid curves) and $\gamma n \to \pi^0 n$ (blue dashed curves) reaction reactions at several photon energies (a) E = 340 MeV, (b) E = 630 MeV, and (c) E = 787 MeV, which correspond to $\Delta(1232)3/2^+$, $N(1440)1/2^+$, and $N(1535)1/2^-$ regions, respectively (Ref. [39]).

The GWU SAID database contains phenomenological amplitudes for the reactions $\pi N \to \pi N$ [40], $NN \to NN$ [41], and $\gamma N \to \pi N$ [42]. The GW-ITEP group, for example, used these amplitudes as inputs to calculate the dominant diagrams of the GWU-ITEP FSI approach. The full Bonn potential [43] was then used for the deuteron description, which includes the Fermi motion of nucleons.

The GWU-ITEP FSI calculations [38] are available over a broad energy range (threshold to E = 2.7 GeV), and for the full CM angular range ($\theta = 0°$ to 180°). Overall, the FSI correction factor $R < 1.00$, while its value varies from 0.70 to 0.90 depending on the kinematics. The behavior of R is very smooth vs. pion production angle. There is a sizable FSI effect from the S-wave part of pp-FSI at small angles.

$R(E, \theta)$ is used as the FSI correction factor for the CLAS quasi-free $\gamma d \to \pi^- pp$ cross section averaged over the laboratory photon energy bin width [44,45]. Note that the FSI correction grows rapidly to the forward direction ($\theta < 30°$). There are currently few measurements in this regime, so the uncertainty due to FSI for this reaction at forward angles does not cause too much concern. The contribution of uncertainty in FSI calculations to the overall systematic normalization uncertainty is estimated to be about 2%–3% (the sensitivity to the deuteron wave-function is 1% and to the number of steps in the integration of the five-fold integrals is 2%). For the CLAS measurements, no sensitivity was found to the value of proton momentum used to determine whether or not it is a spectator.

The $\gamma n \to \pi^0 n$ measurement is much more complicated than the case of $\gamma n \to \pi^- p$ because the π^0 can come from both neutron and proton initial states. The GW-ITEP studies have shown that photoproduction cross sections from protons and neutrons are generally not equal [39]. For π^0 photoproduction on proton and neutron targets we have

$$A(\gamma p \to \pi^0 p) = A_v + A_s \quad \text{and} \quad A(\gamma n \to \pi^0 n) = A_v - A_s, \tag{14}$$

where A_v and A_s are the isovector and isoscalar amplitudes, respectively. Therefore, if $A_s \neq 0$ the γp and γn amplitudes are not equal.

Fig. 5 shows that proton and neutron cross sections are very close to each other in the $\Delta(1232)3/2^+$ region ($A_s = 0$). At higher energies, however, the contributions from $N(1440)1/2^+$ and $N(1535)1/2^-$ become important, the isoscalar amplitude does not equal zero, and the difference between proton and neutron differential cross sections becomes more clearly visible. That means in general that one cannot simply use the ratio between free and bound proton data to be indicative of the ratio between free and bound neutron data. Measurements using bound neutrons will thus always carry significant model-dependent uncertainty.

Unfortunately, there are currently no FSI calculations for polarized measurements on neutron targets. In the absence of these calculations, for PWA one can only assume that the effects of FSI on polarization observables are small. There is some indirect proof that this assumption is reasonable, since several PWAs can successfully fit the polarized measurements in the world database (see, for instance, [46,47]).

Please cite this article as: D.G. Ireland, E. Pasyuk and I. Strakovsky, Photoproduction reactions and non-strange baryon spectroscopy, Progress in Particle and Nuclear Physics (2019) 103752, https://doi.org/10.1016/j.ppnp.2019.103752.

4. Experimental facilities

In this section, we provide a brief description of, and references to, the experimental facilities that were the main contributors of photoproduction data over the last two decades. Some of the facilities used bremsstrahlung to generate real photons, others used laser Compton backscattering. Some detectors were optimized for charged particles, others for neutrals. In that respect they are all complimentary to one another.

4.1. CEBAF

The Thomas Jefferson National Accelerator Facility (TJNAF) commonly known as Jefferson Lab or JLab is the home of the Continuous Electron Beam Accelerator Facility, CEBAF. This is a race track shaped machine that consists of two linear accelerators joined together with a pair of arc sections. For the results reported here, the electron beam made up to five passes through the machine and gained an energy up to 6 GeV, and could be highly polarized. The extracted beam was delivered to end stations known as Hall A, Hall B and Hall C. The majority of photoproduction data at CEBAF was obtained in Hall B with the CLAS detector.

Recently CEBAF was upgraded and its energy doubled, so it can now accelerate electrons up to 12 GeV. One more experimental hall, Hall D, was added.

4.1.1. CLAS

The CEBAF Large Acceptance Spectrometer (CLAS) was a magnetic spectrometer with a toroidal magnetic field [48] that was operational until 2012. It has since been upgraded to CLAS12 to cope with the increased electron beam energy in Hall B. The new detector has a slightly different configuration to the older CLAS, although some of the original detector subsystems have been refurbished and retained. The toroidal field bends particles of different charge either towards or away from the beam direction, which results in some asymmetry of the acceptance for opposite charges. The magnetic field of CLAS was produced by six superconducting coils positioned around the beam, and it could essentially be considered as six independent spectrometers. The gaps between each pair of the coils were filled with detector packages, each of which had six multilayer drift chambers for charged particle tracking. The momentum resolution for charge particles from tracking depended on the angle and magnetic field setting and on average was $\Delta p/p \sim 0.5 - 1\%$. The polar angle resolution was about 1 mrad or better, whilst the azimuthal angle resolution was about 4 mrad. The drift chambers were followed by gas Čerenkov counters for electron pion separation, covering forward angles up to 45°. Further out there was an array of TOF scintillation counters that were used for charged particle identification. The TOF counters covered the polar angle range from 8° to 142° and the full range of azimuthal angles. The solid angle for charged particles was about 60% of 4π. The last detector in a package was an electromagnetic calorimeter, which was a sampling calorimeter made of alternating layers of lead and plastic scintillators. The total thickness was 16 radiation lengths, and the sampling fraction was approximately 0.3 for electrons of 3 GeV and greater. For smaller energies, there was a monotonic decrease to about 0.25 for electrons of 0.5 GeV. The energy resolution was $\sigma/E = 10.3\%/\sqrt{E(\text{GeV})}$. In order to get the coordinates of the shower the scintillator strips were arranged to provide three views crossing each other at 60°. The calorimeters covered angles from 8° to 45°. The design of CLAS was optimized for charged particles.

The unpolarized or circularly polarized photons were produced via bremsstrahlung on a thin gold foil. Coherent bremsstrahlung on a diamond radiator was used to produce linearly polarized photons. Tagging of bremsstrahlung photons was done by the Hall B tagging spectrometer [49], with a tagging range from 20% to 95% of the electron beam energy. The focal plane was instrumented with a two-layer scintillation hodoscope. The first layer consisted of 384 overlapping counters, providing the energy of the post-bremsstrahlung electron with an accuracy of ~ 0.001 of the electron beam energy. The second layer of 61 counters provided timing information.

The target was placed in the center of the detector and was surrounded by a scintillation start counter. CLAS could operate with various types of targets: unpolarized gas, liquid and solid targets. Two different frozen spin polarized targets were used in photoproduction experiments. One, FROST [50], with butanol as a target material, was used for experiments with polarized protons. It allowed for longitudinal and transverse polarization of protons. The second target, HDIce [51], was used for experiments with longitudinally polarized protons and deuterons.

4.2. ESRF

The European Synchrotron Radiation Facility (ESRF) is the most intense source of synchrotron-generated light. After the ESRF pre-injector LINAC, 200 MeV electrons are injected into the booster synchrotron which accelerates them to 6 GeV. They are then injected into a 6 GeV storage ring, where they can be used for physics experiments.

Please cite this article as: D.G. Ireland, E. Pasyuk and I. Strakovsky, Photoproduction reactions and non-strange baryon spectroscopy, Progress in Particle and Nuclear Physics (2019) 103752, https://doi.org/10.1016/j.ppnp.2019.103752.

4.2.1. GRAAL

One of the collaborative research beam lines at ESRF hosted the GRenoble Anneau Accélérateur Laser (GRAAL) facility [52]. Photons were produced by Compton backscattering of laser light from the electron beam. The tagged photon energy spectrum at GRAAL extended from 600 MeV to 1500 MeV. The core of the facility was a large solid angle detector (Laγrange). The central part of Laγrange was a BGO calorimeter, which covered polar angles 25°–155° and full range of azimuthal angle. In the center of the calorimeter there was a plastic scintillator barrel and internal tracker made of two cylindrical multiwire proportional chambers (MWPC). The forward polar angles below 25° were covered by two pairs of planar MWPCs and a double wall of plastic scintillators, followed by a shower wall consisting of four layers of lead and plastic scintillators. The calorimeter had excellent energy resolution for photons and electrons, 3% at 1 GeV, and had a good response for protons below 300 MeV. Charged particles could be tracked by MWPCs, whereas neutrons could be detected either in a BGO calorimeter or the forward wall. The entire apparatus was optimized for the detection of mesons decaying to photons, but could also detect charged particles. GRAAL is no longer in operation, and the BGO calorimeter has been moved to Bonn to become part of the new BGO-OD setup [53].

4.3. MAMI

The Mainz Microtron, MAMI, is a continuous wave accelerator system for electron beams, run by the Institute for Nuclear Physics at the University of Mainz, which is used extensively for hadron physics experiments. Over the years it has been through a series of upgrades, the latest incarnation of which is MAMI-C, which can accelerate electrons up to 1508 MeV. The experimental area A2 is dedicated to experiments with tagged bremsstrahlung photons. Linearly polarized photons are produced via coherent bremsstrahlung on a diamond radiator. Photon tagging is done by the Glasgow tagger [54], which was originally built for MAMI-B with maximum energy of 833 MeV. To improve energy resolution it was later complemented by a microscope [55] with increased energy resolution over a smaller range of electron energies. After MAMI-C commenced operation, the tagger was upgraded for use with beams of energies up to 1500 MeV [56], and has a tagging range is 5%–93% of the full electron beam energy. The energy resolution without the microscope is 4 MeV for a 1500 MeV incident beam, whilst the microscope improves the energy resolution by a factor of 6 in the 60 MeV energy range.

4.3.1. DAPHNE

DAPHNE (Detecteur à grande Acceptance pour la PHysique photoNucleaire Experimentale) was a large acceptance tracking detector for intermediate-energy hadrons comprising a vertex detector surrounded by a segmented calorimeter [57]. The detector consisted of three principal parts, arranged as a coaxial set. In the center there was a vertex detector, surrounded by a charged-particle detector consisting of several layers of scintillator, which was itself surrounded by a lead–aluminium–scintillator sandwich designed to detect neutral particles. It covered polar angles from 21° to 159° and had full azimuthal angle coverage. DAPHNE is no longer in operation.

4.3.2. TAPS

TAPS (the Two Arm Photon Spectrometer) [58] is a detector array originally consisting of 384 individual modules of hexagonal shaped detectors. Each detector module is a telescope consisting of a BaF_2 crystal and a separate plastic scintillator in front of it. It can be used for charged/neutral separation and charged particle identification, with an energy resolution of $\sigma/E = 0.59\%/\sqrt{E_\gamma} + 1.9\%$, where E_γ is given in GeV, and a position resolution of about 2 cm. TAPS was originally designed to detect the two photon decays of π^0 and η mesons. By the year 2006 the number of crystals increased to 600 from the original 384. Recently TAPS was split in two parts, to be used separately with other detectors: the Crystal Ball and the Crystal Barrel.

4.3.3. Crystal Ball/TAPS

The most recent experimental setup in A2 is a combination of the Crystal Ball and half of TAPS. The details of this configuration of the setup can be found in Ref. [59]. The Crystal Ball was originally built by the Stanford Linear Accelerator Center (SLAC) [60], and consists of 672 optically isolated NaI(Tl) crystals, with a thickness of 15.7 radiation lengths. The crystals are arranged to form a sphere covering 93% of the full solid angle. The energy resolution for electromagnetic showers is given by $\Delta E/E = 0.02/(E/\mathrm{GeV})^{0.36}$. The accuracy of the shower direction reconstruction is about $\sigma_\theta \sim 2$–$3°$ for polar angles and $\sigma_\varphi \sim 2°/\sin\theta$ for azimuthal angles. In the center of the Crystal Ball is a barrel of 24 scintillation counters surrounding the target, which measures energy losses of the charged particle and can be used in $\Delta E/E$ analysis for charged particles identification, and is also used to separate charged particles from neutrals. The forward angles $\theta = 1$–$20°$ are covered by one half of TAPS, which is placed 1.5 m downstream of the Crystal Ball center. The combined solid angle of the Crystal Ball and TAPS is 97% of 4π. This setup can be used with both polarized and unpolarized targets. This facility is operational and continues data taking.

Please cite this article as: D.G. Ireland, E. Pasyuk and I. Strakovsky, Photoproduction reactions and non-strange baryon spectroscopy, Progress in Particle and Nuclear Physics (2019) 103752, https://doi.org/10.1016/j.ppnp.2019.103752.

4.4. ELSA

The electron accelerator ELektronen-Stretcher-Anlage (ELSA) [61] is operated by the University of Bonn. It has three stages: injector LINACs, a booster synchrotron and a stretcher ring. It can deliver beams of polarized or unpolarized electrons with energies up to 3.5 GeV. Real photon beams are produced via bremsstrahlung, and a linearly polarized beam is produced via coherent bremsstrahlung. The bremsstrahlung photons are tagged with a tagging hodoscope, resulting in an accuracy of the photon energy of 0.4% of the electron beam energy.

4.4.1. SAPHIR

SAPHIR (Spectrometer Arrangement for PHoton Induced Reactions) [62] was a large solid angle detector at the Bonn accelerator ELSA, with a magnetic spectrometer with a dipole magnet. The photon beam entered through a hole in the magnet yoke, and the space between the magnet poles was occupied by the Central Drift Chamber (CDC) for charged particle tracking. The target was placed in the center of the CDC. For better tracking and momentum resolution there were also three planar drift chambers, two on the sides and one in the forward direction. The momentum resolution of about 6.5% was achieved at 1.0 GeV/c particle momentum, but the use of the forward drift chamber improved the momentum resolution considerably; up to 2% at 1.8 GeV/c. There were three planes of scintillation counter hodoscopes: two on the sides and one in the forward direction. The hodoscopes in coincidence with the tagging system produced the trigger and were used for particle identification by measuring time-of-flight (TOF). Downstream of the forward TOF there was an array of electromagnetic shower counters (EMC), whose energy resolution was found to be $13\%/\sqrt{E}$, where E is in GeV. SAPHIR is no longer in operation.

4.4.2. CBELSA

The central part of the setup is the Crystal Barrel [63], a calorimeter that was originally used at the Low Energy Antiproton Ring (LEAR) at CERN. In its original configuration it consisted of 1380 CsI(Tl) crystals, each of which was 16.1 radiation lengths. The crystals are grouped in 26 rings ($\Delta\theta = 6^\circ$), where the larger rings consist of 60 crystals ($\Delta\varphi = 6^\circ$); the six smallest rings contain 30 crystals ($\Delta\varphi = 12^\circ$). It covers angles from 12° to 168° with respect to the beam direction, resulting in 97.8% coverage of the solid angle. During the first configuration change the three forward rings were taken out and TAPS was installed as a forward wall to extend coverage to smaller angles down to 1°. During the second configuration change the forward crystals ($\theta < 27^\circ$) were covered by plastic scintillators in front of each crystal for charged particle identification. The most forward angles were covered by miniTAPS. Inside the calorimeter, a three-layer inner detector with 513 scintillating fibers was installed. In the current configuration all of the Crystal Barrel is instrumented with APD readout for better trigger capability. More details on the most recent version of the setup can be found in Ref. [64]. This setup is optimized for detection of multiphoton events. CBELSA is active and continues data taking.

4.4.3. BGO-OD

The BGO-OD [53] is a new experiment at ELSA. It consists of a central detector enclosing the target in the angular range 10–155°, and is complemented by a large aperture forward magnetic spectrometer covering the angular range from approximately 2° to 12°. The main component of the central detector is the BGO calorimeter formerly used at GRAAL. A segmented plastic scintillator barrel and a double layer cylindrical MWPC are placed inside the calorimeter to enable tracking and identification of charged particles. The forward spectrometer consists of a large aperture dipole magnet sandwiched between tracking detectors. Front tracking upstream of the magnet is performed with two sets of scintillating fiber detectors. Eight double layers of drift chambers serve for rear tracking downstream of the magnet. The BGO-OD was commissioned in 2016.

4.5. SPring-8

SPring-8 is a large synchrotron radiation facility located in Harima Science Park City, Japan. The name "SPring-8" is derived from "**S**uper **P**hoton **ring-8** GeV". As the name implies, it is an 8 GeV electron storage ring. Among many other applications it is used for hadronic physics, and photoproduction in particular.

4.5.1. LEPS

The backward Compton scattering of laser light from a high energy electron beam is used to produce high energy photons. This type of beam line was constructed at Spring-8 and is termed the "Laser-electron-photon" (LEP) facility. If the laser light is polarized then the high energy photons that are produced are also polarized. The photons were tagged by detecting scattered electrons. The initial version of this facility could provide photons with energies up to 2.4 GeV. The first detector, LEPS [65], was designed to study ϕ-meson photoproduction at forward angles. It was a magnetic spectrometer with a dipole magnet. The vertex detector was located upstream of the magnet and consists of silicon strip detectors and drift chambers. Downstream of the magnet there were two sets of drift chambers, one on each side of the beam. Particle identification was done using TOF. The LEP beam line has been upgraded to increase the intensity of the photon beam and extend the energy range up to 2.9 GeV [66].

Please cite this article as: D.G. Ireland, E. Pasyuk and I. Strakovsky, Photoproduction reactions and non-strange baryon spectroscopy, Progress in Particle and Nuclear Physics (2019) 103752, https://doi.org/10.1016/j.ppnp.2019.103752.

4.5.2. LEPS2

The same approach was used to construct the second LEP beam line, LEPS2 [67]. LEPS1 had an acceptance limited to forward angles only. To overcome this limitation, new detectors were needed to be constructed for LEPS2. One of the detectors that aimed to study η' mesic nuclei is BGOegg [68]. The detector is optimized for detection of photons and is an egg-shaped electromagnetic calorimeter. It consists of 1320 BGO crystals of 20 radiation lengths. It has a polar angle coverage from 24° to 144° and complete azimuthal coverage. The energy resolution is 1.3% at 1 GeV and the position resolution is 3.1 mm. To detect charged particles the scintillation hodoscopes and cylindrical drift chambers are installed in the center of the calorimeter.

The second detector for LEPS2 is a solenoid spectrometer [67]. It is designed to detect both charged particles and photons. It is a solenoid magnet with a 0.9 T field, where tracking of charged particles is done by the time projection chamber (TPC) and forward drift chambers. The tracking detectors are surrounded by a barrel of resistive plate chambers (RPC) that have very good timing resolution and are used for particle identification by measuring TOF. For particle momenta above 1 GeV, in addition to TOF the aerogel Čerenkov counters are used. The outer most detector is a barrel electromagnetic calorimeter, Barrel γ, which is a sampling lead/plastic scintillator calorimeter with a thickness of 14.3 radiation lengths and covers polar angles 30–110°.

4.6. ELPH

The Research Center for ELectron PHoton Science (ELPH), formerly the Laboratory for Nuclear Science (LNS), was established in 1966 and attached to the Faculty of Science, Tohoku University. ELPH presently has two electron linacs, one of which, a high intensity 70 MeV linac, is used for radio isotope production. The second one, a 90 MeV linac, is used as an injector for the 1.3 GeV Booster STorage ring (BST) [69], which is a synchrotron that can accelerate electrons up to 1.3 GeV. The BST can operate in two modes: as a stretcher or as a storage ring. There are two tagged photon beam lines [70]. One of these hosts the Neutral Kaon Spectrometer 2 (NKS2) [71], whilst the other was equipped with the large electromagnetic calorimeter array FOREST [72].

4.6.1. NKS2

The NKS2 was designed to study strangeness photoproduction. It consists of a dipole magnet, whose magnetic field is 0.42 T at the center. The liquid target cell is installed in the center of the magnet and is surrounded by two sets of drift chambers: Cylindrical Drift Chambers (CDC) and Vertex drift Chambers (VDC) for charged particle tracking in the magnetic field. Two scintillation hodoscopes, the Inner Hodoscope (IH) and the Outer Hodoscope (OH) are used for time-of-flight measurement.

4.6.2. FOREST

A large solid angle detector system FOREST was designed to study π^0 and η photoproduction. It consists of three different types of electromagnetic calorimeters covering different angular ranges. The first, covering forward angles of 4-24°, is made of 192 pure CsI crystals. The second one covers intermediate angles from 30° to 100°, and consists of 252 lead scintillation fiber (Lead/SciFi) blocks. The last one, covering backward angles of 110° to 175°, is an array of 62 lead glass Čherenkov counters. Scintillation hodoscope was placed in front of the calorimeters, and was used for charge/neutral particle identification.

5. Available experimental data on meson photoproduction

In this section, we give an overview of available experimental data of meson photoproduction. The source of the data for single meson production is the SAID database [15] which is to date the most comprehensive. The SAID database does not contain data for two-meson photoproduction. Some of the data can be found in HEPdata database [73]. The CLAS Collaboration maintains its own database [74], but this only contains data obtained with the CLAS detector.

The data are organized by the final state. The number of data points accumulated thus far makes it pointless to try to plot each of them in this review. Instead we plot for each channel, in the style of Fig. 1, the number of data points as a function of hadronic mass W, and as a function of year. The data are split into unpolarized and polarized stacked histograms and are meant to convey the relative amount available from each channel, as well as an indication of the progress in measurements over time.

For convenience we list the thresholds for the relevant photoproduction reactions. They can be found in Table 3. Since most of the photoproduction data were obtained within last two decades, we concentrate on this period. We also limit discussion to the center of mass energies $W \leq 2.55$ GeV ($E_\gamma \leq 3$ GeV). Figs. 6 through 16 show energy distributions for 1996 through 2018 (left) and time distributions (right). Tables 4 through 17 provide references to all relevant experiments from 1996 through 2018. They are organized by reaction and include observable, energy and angular range, number of the experimental data and a reference to original publication. We have not included total cross sections because they were not directly measured but obtained by integration of differential ones, and depend on the angular range of differential quantities measurements and extrapolation procedure. For the reaction channels with limited amount of measurements we show only tables. For double meson production we do not provide tables but rather just list experiments, their energy

Please cite this article as: D.G. Ireland, E. Pasyuk and I. Strakovsky, Photoproduction reactions and non-strange baryon spectroscopy, Progress in Particle and Nuclear Physics (2019) 103752, https://doi.org/10.1016/j.ppnp.2019.103752.

Table 3
Threshold energies.

Reaction	W (MeV)	E_γ (MeV)
$\gamma p \to \pi^0 p$	1073.2	144.7
$\gamma n \to \pi^0 n$	1074.5	144.7
$\gamma n \to \pi^- p$	1077.8	148.4
$\gamma p \to \pi^+ n$	1079.1	151.4
$\gamma p \to \eta p$	1487.4	707.6
$\gamma n \to \eta n$	1486.1	707.8
$\gamma p \to K^+ \Lambda$	1609.4	911.1
$\gamma n \to K^0 \Lambda$	1613.3	915.3
$\gamma p \to K^+ \Sigma^0$	1686.3	1046.2
$\gamma p \to K^0 \Sigma^+$	1687.0	1047.4
$\gamma n \to K^0 \Sigma^0$	1690.2	1050.6
$\gamma n \to K^+ \Sigma^-$	1691.1	1052.1
$\gamma n \to \omega n$	1722.2	1108.6
$\gamma p \to \omega p$	1720.9	1109.1
$\gamma p \to \eta' p$	1896.0	1446.6
$\gamma p \to \pi^0 \pi^0 p$	1208.2	308.8
$\gamma p \to \pi^+ \pi^- p$	1217.4	320.7
$\gamma p \to \pi^0 \eta p$	1621.1	931.3

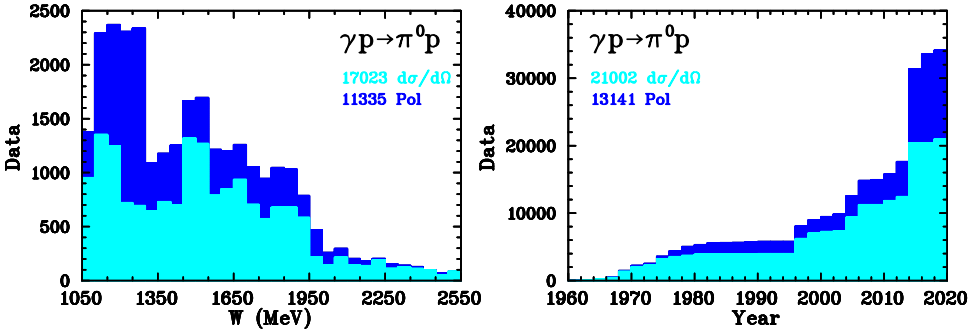

Fig. 6. Database for $\gamma p \to \pi^0 p$. *Left*: Experimental data from the SAID database [15] selected for 1996 through 2018. *Right*: Amount of data as a function of time. Full SAID database. The data shown as stacked histogram. Light shaded – cross sections, dark shaded – polarization data.

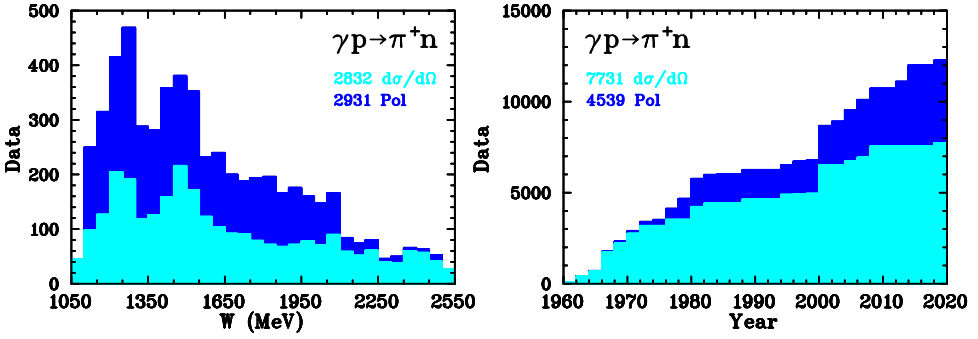

Fig. 7. Database for $\gamma p \to \pi^+ n$. The notation is the same as in Fig. 6.

range and extracted observables, and provide reference to the original publications. The reason for this is the following. Since these are not binary reaction there are many possible choices of kinematic variables. The same data can be binned differently depending on the goal of the analysis. In many cases event by event likelihood analysis was used without any binning.

5.1. Single pion photoproduction

The first experimental study of single pion photoproduction has started just two years after discovery of pion. It has the lowest threshold and at low energies it is dominated by Δ. The amount of data vs. energy essentially follows

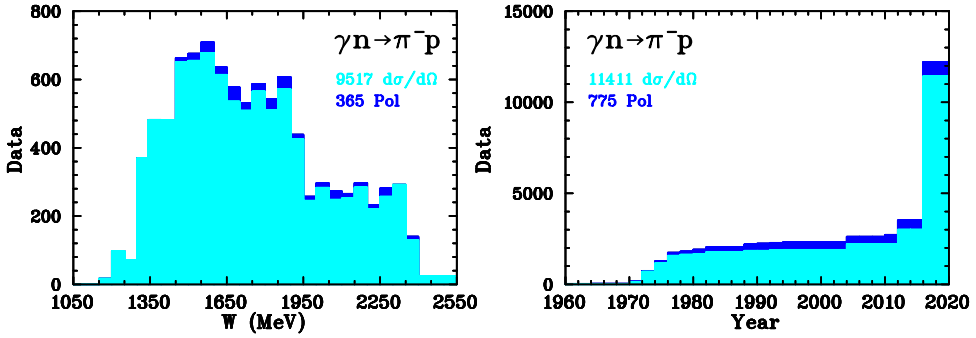

Fig. 8. Database for $\gamma n \to \pi^- p$. The notation is the same as in Fig. 6.

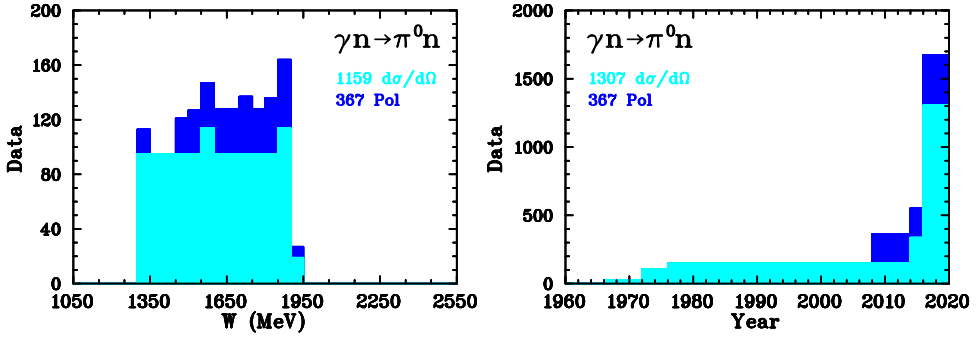

Fig. 9. Database for $\gamma n \to \pi^0 n$. The notation is the same as in Fig. 6.

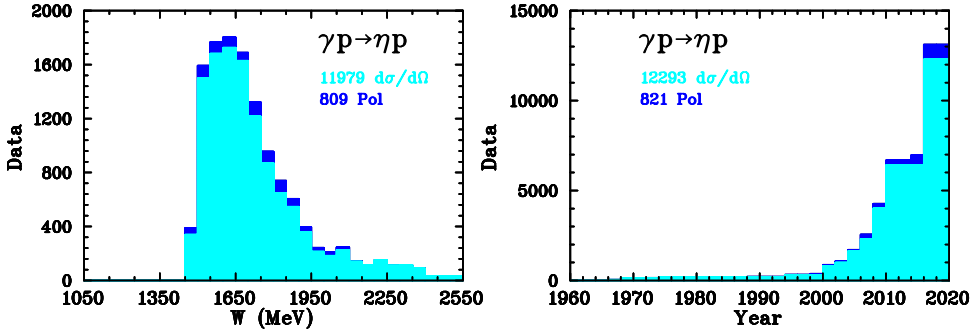

Fig. 10. Database for $\gamma p \to \eta p$. The notation is the same as in Fig. 6.

the cross section For pion photoproduction, there is a large difference between the amount of data from π^0p and π^+n measurements: π^+n/π^0p = 20%. Also pion photoproduction from the neutron is much less known compared to that from the proton, n/p = 31% [15] (see Figs. 6–9).

5.2. η and η' photoproduction

Since η and η' are iso-singlets their photoproduction may not be directly coupled to Δ resonances but only to the excitation of N^*

5.3. Kaon photoproduction

Whilst the cross section for kaon photoproduction is a couple of orders of magnitude smaller than pion photoproduction, these channels have been seen as the "golden" channels in recent times for a number of reasons. A different coupling of kaons to light baryon resonances had been hypothesized as a means of discovering more resonances [142]. More importantly, especially with the $K\Lambda$ final state, the self-analyzing property of the Λ through its weak decay means

Please cite this article as: D.G. Ireland, E. Pasyuk and I. Strakovsky, Photoproduction reactions and non-strange baryon spectroscopy, Progress in Particle and Nuclear Physics (2019) 103752, https://doi.org/10.1016/j.ppnp.2019.103752.

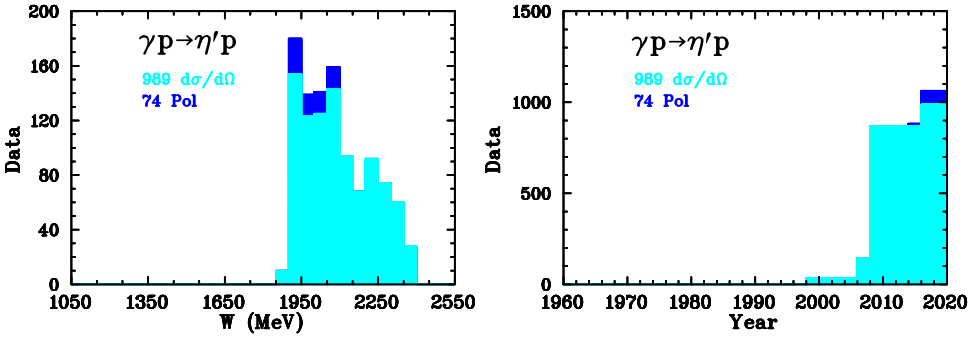

Fig. 11. Database for $\gamma p \to \eta' p$. The notation is the same as in Fig. 6.

Table 4
Data for $\gamma p \to \pi^0 p$ below W = 2.55 GeV (E_γ = 3 GeV). $\Delta_{13} = (d\sigma/d\Omega)_{1/2} - (d\sigma/d\Omega)_{3/2}$. Experimental data are from the SAID database [15] selected for 1996 through 2018. Polarized data contribution is 40%.

Observable	W (MeV)	θ (deg)	Data	Lab	Ref
$d\sigma/d\Omega$	1074–1091	10–170	171	MAMI	[75]
	1075–1136	18–162	600	MAMI	[76]
	1122–1537	3–178	1129	MAMI	[77]
	1131–1227	70–130	73	BNL	[78]
	1136–1957	15–165	7978	MAMI	[79]
	1209–1376	55–120	67	MAMI	[80]
	1217–2439	32–148	1089	ELSA	[81]
	1277–1277	70–178	24	MAMI	[82]
	1386–1942	45–168	861	GRAAL	[83]
	1390–1531	45–119	97	MAMI	[84]
	1455–1538	26–154	799	MAMI	[85]
	1465–2505	41–148	620	CEBAF	[42]
	1810–2542	34–80	580	CEBAF	[86]
	1934–2300	129–167	112	Spring-8	[87]
Σ	1075–1126	25–155	220	MAMI	[76]
	1086–1086	30–150	7	MAMI	[75]
	1131–1306	60–150	84	BNL	[78]
	1154–1306	11–170	353	MAMI	[77]
	1216–1448	31–158	1403	MAMI	[88]
	1349–1702	85–125	158	Yerevan	[89]
	1384–1910	45–171	441	GRAAL	[83]
	1523–1869	37–156	135	ELSA	[90]
	1621–1998	5–165	249	ELSA	[91]
	1717–2091	32–148	700	CEBAF	[92]
	1946–2280	129–167	48	Spring-8	[87]
P	1471–1613	51–163	152	ELSA	[93]
	1527–2349	59–135	29	CEBAF	[94]
	2084–2468	96–143	3	CEBAF	[95]
T	1073–1291	5–175	4343	MAMI	[96]
	1179–1398	53–127	52	ELSA	[97]
	1306–1888	30–162	397	MAMI	[59]
	1471–2479	29–163	601	ELSA	[93]
G	1232–1232	70–110	3	MAMI	[98]
	1438–1822	19–161	318	ELSA	[99]
H	1472–1613	51–163	154	ELSA	[93]
F	1306–1888	30–162	397	MAMI	[100]
E	1426–2259	22–158	456	ELSA	[101]
Δ_{13}	1209–1376	59–122	62	MAMI	[80]
	1390–1531	44–123	78	MAMI	[84]
$C_{x'}$	1322–1841	75–140	45	MAMI	[102]
	1527–2349	59–135	28	CEBAF	[94]
	2084–2468	96–143	3	CEBAF	[95]
$C_{z'}$	1527–2349	59–135	25	CEBAF	[94]
	2084–2468	96–143	3	CEBAF	[95]

Table 5
Data for $\gamma p \to \pi^+ n$ below W = 2.55 GeV (E_γ = 3 GeV). $\Delta_{13} = (d\sigma/d\Omega)_{1/2} - (d\sigma/d\Omega)_{3/2}$. Experimental data are from the SAID database [15] selected for 1996 through 2018. Polarized data contribution is 51%.

Observable	W (MeV)	θ (deg)	Data	Lab	Ref
$d\sigma/d\Omega$	1080–1081	46–134	45	TRIUMF/SAL	[103]
	1104–1313	31–157	205	MAMI	[80]
	1162–1277	72–143	39	MAMI	[104]
	1178–1292	45–135	160	MAMI	[105]
	1193–2201	112–179	1267	ELSA	[106]
	1323–1533	45–155	203	MAMI	[107]
	1497–2505	32–148	618	CEBAF	[108]
	1714–2354	50–90	10	CEBAF	[109]
	1934–2524	11–49	174	Spring-8	[110]
Σ	1178–1292	20–170	85	BNL	[78]
	1178–1292	45–135	160	MAMI	[105]
	1416–1688	48–154	92	GRAAL	[111]
	1543–1901	47–160	237	GRAAL	[112]
	1722–2091	32–148	386	CEBAF	[92]
	1946–2496	11–49	84	Spring-8	[110]
G	1232–1232	30–130	6	MAMI	[98]
E	1250–2230	20–148	900	CEBAF	[113]
Δ_{13}	1104–1313	35–153	129	MAMI	[80]
	1323–1524	50–150	102	MAMI	[107]

Table 6
Data for $\gamma n \to \pi^- p$ below W = 2.55 GeV (E_γ = 3.1 GeV). Experimental data from the SAID database [15] selected for 1996 through 2018. Polarized data contribution is 4%.

Observable	W (MeV)	θ (deg)	Data	Lab	Ref
$d\sigma/d\Omega$	1191–1526	41–148	300	BNL	[114]
	1203–1318	58–133	104	MAMI	[115]
	1311–2366	26–135	8428	CEBAF	[45]
	1690–2551	33–157	699	CEBAF	[116,117]
	1720–2356	50–90	1	CEBAF	[109]
Σ	1516–1894	33–163	99	GRAAL	[118]
E	1500–2300	26–154	266	CEBAF	[46]

Table 7
Data for $\gamma n \to \pi^0 n$ below W = 2.55 GeV (E_γ = 3 GeV). Experimental data are from the SAID database [15] selected for 1996 through 2018. Polarized data contribution is 24%.

Observable	W (MeV)	θ (deg)	Data	Lab	Ref
$d\sigma/d\Omega$	1300–1900	32–162	969	MAMI	[47]
Σ	1484–1912	53–164	216	GRAAL	[119]
E	1312–1888	46–154	151	MAMI	[47]

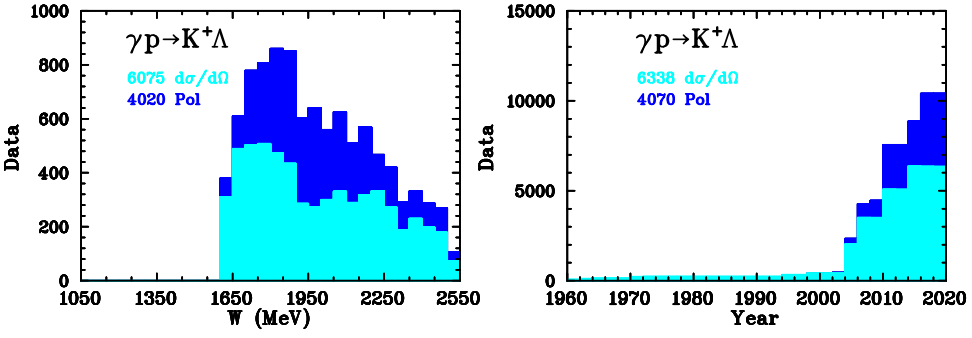

Fig. 12. Database for $\gamma p \to K^+ \Lambda$. The notation is the same as in Fig. 6.

that information on the recoil polarization is readily obtainable in the final state. Together with the advances in photon beam and target polarization, this has meant that a large number of polarization observables have been extracted across the resonance region. Such data have been shown to be extremely useful in fitting model parameters and establishing the existence of resonances.

Please cite this article as: D.G. Ireland, E. Pasyuk and I. Strakovsky, Photoproduction reactions and non-strange baryon spectroscopy, Progress in Particle and Nuclear Physics (2019) 103752, https://doi.org/10.1016/j.ppnp.2019.103752.

Table 8
Data for $\gamma p \to \eta p$ below W = 2.55 GeV (E_γ = 3.1 GeV). $\Delta_{13} = (d\sigma/d\Omega)_{1/2} - (d\sigma/d\Omega)_{3/2}$. Experimental data are from the SAID database [15] selected for 1996 through 2018. Polarized data contribution is 6%.

Observable	W (MeV)	θ (deg)	Data	Lab	Ref
$d\sigma/d\Omega$	1488–1870	18–162	2400	MAMI	[120]
	1488–1957	17–163	5880	MAMI	[121]
	1490–1911	32–162	487	GRAAL	[122]
	1492–1739	26–154	180	ELPH	[123]
	1528–2120	46–134	190	CEBAF	[124]
	1528–2120	33–148	1012	CEBAF	[125]
	1533–2510	18–139	631	ELSA	[126]
	1533–1537	70–70	2	MAMI	[127]
	1685–2370	18–162	680	ELSA	[128]
	1994–2300	130–162	32	Spring-8	[129]
Σ	1496–1909	33–161	150	GRAAL	[122]
	1569–1845	51–148	34	ELSA	[130]
	1700–2080	46–134	201	CEBAF	[131]
T	1492–1719	33–145	50	ELSA	[97]
	1497–1848	24–156	144	MAMI	[132]
F	1497–1848	24–156	144	MAMI	[132]
E	1525–2125	46–154	69	CEBAF	[133]
Δ_{13}	1533–1537	70–70	129	MAMI	[127]

Table 9
Data for $\gamma n \to \eta n$ below W = 2.55 GeV (E_γ = 3 GeV). Experimental data are from the SAID database [15] selected for 1996 through 2018. Polarized data contribution is 15%.

Observable	W (MeV)	θ (deg)	Data	Lab	Ref
$d\sigma/d\Omega$	1483–2322	26–154	200	ELSA	[134]
	1487–2070	51–151	279	ELSA	[135]
	1492–1875	18–162	880	MAMI	[136]
Σ	1506–1894	32–165	99	GRAAL	[137]
E	1505–1882	37–143	135	MAMI	[138]

Table 10
Data for $\gamma p \to \eta' p$ below W = 2.55 GeV (E_γ = 3 GeV). Experimental data are from the SAID database [15] selected for 1996 through 2018. Polarized data contribution is 7%.

Observable	W (MeV)	θ (deg)	Data	Lab	Ref
$d\sigma/d\Omega$	1898–1956	26–154	120	MAMI	[121]
	1917–2336	37–143	34	ELSA	[139]
	1925–2380	32–146	524	CEBAF	[125]
	1934–2350	26–154	200	ELSA	[128]
	1935–2249	46–134	111	CEBAF	[140]
Σ	1903–1912	20–159	14	GRAAL	[141]
	1904–2080	46–134	60	CEBAF	[131]

The plot in Fig. 12 indicates that very few kaon photoproduction data were available before the start of the century. Initial measurements by SAPHIR [143,144], SPring-8 [145–147] and GRAAL [148,149] have been added to by a comprehensive campaign of measurements by CLAS [150–154].

It should be noted that, at the time of writing, a recently published paper by the BES Collaboration [157], and a study of kaon photoproduction at CLAS [158] have cast doubt on the previously quoted value of the weak decay parameter α_- of the Λ. The value obtained by both analyses is significantly higher than the number quoted in the current PDG [34]. As such, this means that the polarization observables that depend on α_- (beam asymmetry, beam–recoil observables) could be systematically too high, and analyses that depend on a fit to them should be examined to establish whether this change would make a difference to the final results (see Figs. 13–15).

5.4. ω Photoproduction

There was no ω photoproduction data before 2003, but a substantial amount has been accumulated since then. All major facilities (CLAS, CBELSA, Crysta Ball at MAMI, GRAAL) made contributions. Based on these data it was found that excitation of nucleon resonances plays an important role in ω photoproduction. The quality of the data near threshold

Table 11
Data for $\gamma p \rightarrow K^+\Lambda$ below W = 2.55 GeV (E_γ = 3 GeV). Experimental data are from the SAID database [15] selected for 1996 through 2018. Polarized data contribution is 40%.

Observable	W (MeV)	θ (deg)	Data	Lab	Ref
$d\sigma/d\Omega$	1610–2390	18–162	701	ELSA	[144]
	1612–1896	66–143	1306	MAMI	[155]
	1617–2290	32–148	920	CEBAF	[150]
	1617–2108	26–154	90	ELSA	[143]
	1625–2395	27–154	1674	CEBAF	[152]
	1628–2533	26–143	1377	CEBAF	[156]
	1934–2310	13–41	78	Spring-8	[145]
Σ	1649–1906	31–144	66	GRAAL	[148]
	1721–2180	37–134	314	CEBAF	[154]
	1946–2300	13–49	45	Spring-8	[146]
	1946–2280	13–49	30	Spring-8	[145]
	2041–2238	18–32	4	Spring-8	[147]
P	1617–2290	26–154	233	CEBAF	[150]
	1625–2545	26–143	1497	CEBAF	[152]
	1649–1906	31–144	66	GRAAL	[148]
	1660–2017	41–139	12	ELSA	[143]
	1660–2280	34–146	30	ELSA	[144]
	1721–2180	37–134	314	CEBAF	[154]
T	1649–1906	31–144	66	GRAAL	[149]
	1721–2180	37–134	314	CEBAF	[154]
$C_{x'}$	1678–2454	32–139	144	CEBAF	[151]
$C_{z'}$	1678–2454	32–139	146	CEBAF	[151]
O_x	1649–1906	31–144	66	GRAAL	[149]
	1721–2180	37–134	314	CEBAF	[154]
O_z	1649–1906	31–144	66	GRAAL	[149]
	1721–2180	37–134	314	CEBAF	[154]

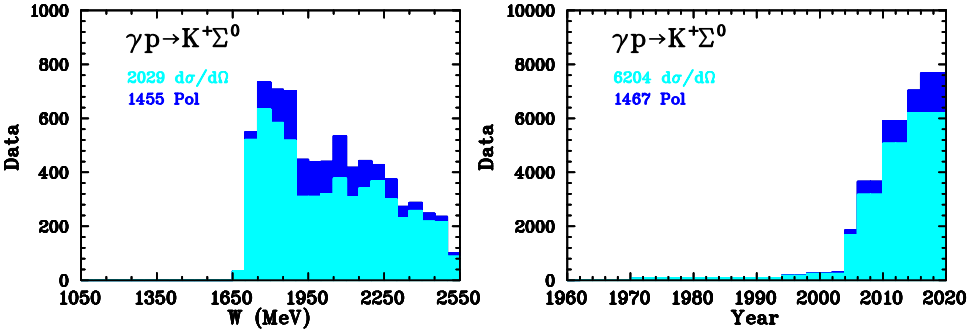

Fig. 13. Database for $\gamma p \rightarrow K^+\Sigma^0$. The notation is the same as in Fig. 6.

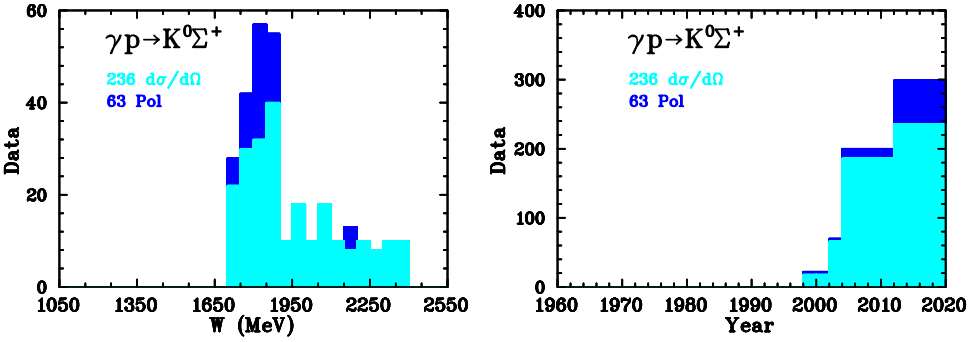

Fig. 14. Database for $\gamma p \rightarrow K^0\Sigma^+$. The notation is the same as in Fig. 6.

Please cite this article as: D.G. Ireland, E. Pasyuk and I. Strakovsky, Photoproduction reactions and non-strange baryon spectroscopy, Progress in Particle and Nuclear Physics (2019) 103752, https://doi.org/10.1016/j.ppnp.2019.103752.

Table 12
Data for $\gamma p \rightarrow K^+\Sigma^0$ below W = 2.55 GeV (E_γ = 3 GeV). Experimental data are from the SAID database [15] selected for 1996 through 2018. Polarized data contribution is 42%.

Observable	W (MeV)	θ (deg)	Data	Lab	Ref
$d\sigma/d\Omega$	1695–2545	26–180	1576	CEBAF	[153]
	1695–2390	18–162	656	ELSA	[144]
	1702–2290	32–139	778	CEBAF	[150]
	1703–1896	66–143	1130	MAMI	[155]
	1713–2533	26–143	1279	CEBAF	[156]
	1716–2370	26–154	120	ELSA	[159]
	1716–2097	26–154	920	ELSA	[143]
	1934–2310	13–41	78	Spring-8	[145]
	1934–2310	18–49	144	Spring-8	[160]
Σ	1737–2170	37–124	127	CEBAF	[154]
	1755–1906	18–138	42	GRAAL	[148]
	1822–2185	37–143	10	ELSA	[159]
	1946–2300	13–49	45	Spring-8	[146]
	1946–2280	13–49	30	Spring-8	[145]
	1946–2300	13–49	72	Spring-8	[160]
P	1728–2550	27–163	355	CEBAF	[153]
	1737–2170	37–124	127	CEBAF	[154]
	1743–2029	41–139	12	ELSA	[143]
	1743–2280	41–139	16	ELSA	[144]
	1756–2290	26–134	97	CEBAF	[150]
	1762–1851	39–130	8	GRAAL	[148]
T	1737–2170	37–124	127	CEBAF	[154]
C_x	1787–2454	37–134	71	CEBAF	[151]
C_z	1787–2454	37–134	72	CEBAF	[151]
O_x	1737–2170	37–124	127	CEBAF	[154]
O_z	1737–2170	37–124	127	CEBAF	[154]

Table 13
Data for $\gamma p \rightarrow K^0\Sigma^+$ below W = 2.55 GeV (E_γ = 3 GeV). Experimental data are from the SAID database [15] selected for 1996 through 2018. Polarized data contribution is 21%.

Observable	W (MeV)	θ (deg)	Data	Lab	Ref
$d\sigma/d\Omega$	1730–1885	29–151	50	MAMI	[161]
	1743–1898	20–156	18	ELSA	[162]
	2062–2263	46–134	48	ELSA	[159]
P	1730–1885	29–151	49	MAMI	[161]
	1822–1822	30–150	4	ELSA	[162]
	2073–2073	30–150	4	ELSA	[159]

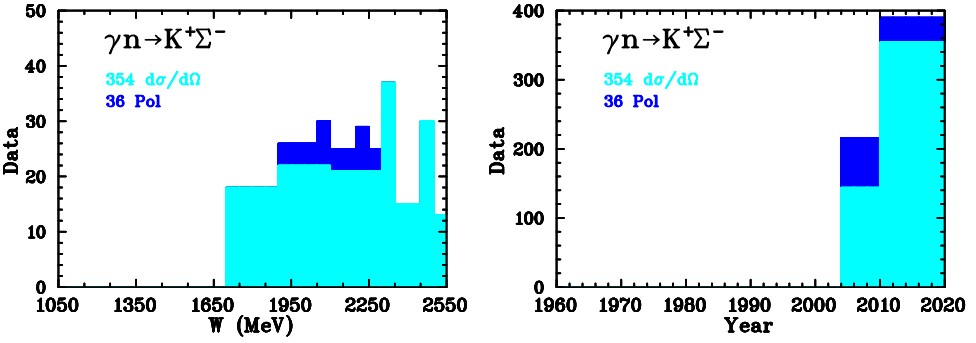

Fig. 15. Database for $\gamma n \rightarrow K^+\Sigma^-$. The notation is the same as in Fig. 6.

gives access to a variety of interesting physics aspects. As an example, an estimation of the ωN scattering length $\alpha_{\omega p}$ is provided [166] (see Table 18).

5.5. Photoproduction of two pseudoscalar mesons

As photon energy increases all the single meson production cross sections decline, but the two pion cross section increases, followed by $\eta\pi$ etc. Once we get above 1.6 GeV two pion production becomes dominant. The two meson final

Table 14
Data for $\gamma n \to K^+\Sigma^-$ below W = 2.55 GeV (E_γ = 3 GeV). Experimental data are from the SAID database [15] selected for 1996 through 2018. Polarized data contribution is 9%.

Observable	W (MeV)	θ (deg)	Data	Lab	Ref
$d\sigma/d\Omega$	1745–2535	34–151	285	CEBAF	[163]
	1934–2310	18–49	144	Spring-8	[160]
Σ	1946–2300	13–49	36	Spring-8	[160]

Table 15
Data for $\gamma n \to K^0\Lambda$ below W = 2.55 GeV (E_γ = 3 GeV). Experimental data are from the SAID database [15] selected for 1996 through 2018. There are no unpolarized measurements.

Observable	W (MeV)	θ (deg)	Data	Lab	Ref
$d\sigma/d\Omega$	1645–2516	41–130	360	CEBAF	[164]
E	1700–2020	53–127	6	CEBAF	[165]

Table 16
Data for $\gamma n \to K^0\Sigma^0$ below W = 2.55 GeV (E_γ = 3 GeV). Experimental data are from the SAID database [15] selected for 1996 through 2018. There are no unpolarized measurements.

Observable	W (MeV)	θ (deg)	Data	Lab	Ref
E	1700–2020	53–127	6	CEBAF	[165]

Table 17
Data for $\gamma p \to \omega p$ below W = 2.55 GeV (E_γ = 3 GeV). SDME is spin-density matrix element. Experimental data are from the SAID database [15] selected for 1996 through 2018. Polarized data contribution is 72%.

Observable	W (MeV)	θ (deg)	Data	Lab	Ref.
$d\sigma/d\Omega$	1723–2380	13–159	307	ELSA	[167]
	1725–2545	24–147	1148	CEBAF	[168]
	1725–1872	21–159	300	MAMI	[166]
	1736–2131	18–139	121	ELSA	[169]
	1756–2350	11–162	648	ELSA	[170]
Σ	1720–2017	19–151	31	ELSA	[171]
	1743–2174	15–145	81	CEBAF	[172]
	1744–2098	32–148	492	CEBAF	[173]
	1750–1903	13–167	28	GRAAL	[174]
P	1150–2050	53–180	50	CEBAF	[175]
T	1796–2458	37–180	143	CEBAF	[172]
G	1778–1778	37–141	5	ELSA	[176]
E	1743–2300	29–151	104	CEBAF	[177]
	1749–2256	28–151	95	ELSA	[176]
F	1250–2750	37–180	160	CEBAF	[175]
H	1150–2050	53–180	50	CEBAF	[175]
SDME	1725–2545	23–147	4592	CEBAF	[125]
	1756–2350	18–151	891	ELSA	[170]

Table 18
Data for $\gamma n \to \omega n$ below W = 2.55 GeV (E_γ = 3 GeV). Experimental data are from the SAID database [15] selected for 1996 through 2018. There are no polarized measurements.

Observable	W (MeV)	θ (deg)	Data	Lab	Ref.
$d\sigma/d\Omega$	1762–2136	18–139	91	ELSA	[169]

state provides a link to the final states $N\rho$, $N\sigma$, and more complex states such as $N^*\pi$, $\Delta\pi$, $\Delta\eta$ etc. The latter final states may result from the excitation of a higher mass resonance, with a sequential decay chain to an intermediate lighter resonance and one meson, followed by the decay to the ground state nucleon and a second meson.

The first total cross section measurements of $\pi^+\pi^-$ photoproduction were carried out in the late 1960s with untagged photon beams of energies up to 1 GeV incident on bubble chambers [178,179]. The critical requirement for double meson production experiments is large solid angle coverage, the capability of detecting multiparticle events and high energy beams of tagged photons. This only became available in the mid 90 s. The first "new era" electronic experiment measuring

Please cite this article as: D.G. Ireland, E. Pasyuk and I. Strakovsky, Photoproduction reactions and non-strange baryon spectroscopy, Progress in Particle and Nuclear Physics (2019) 103752, https://doi.org/10.1016/j.ppnp.2019.103752.

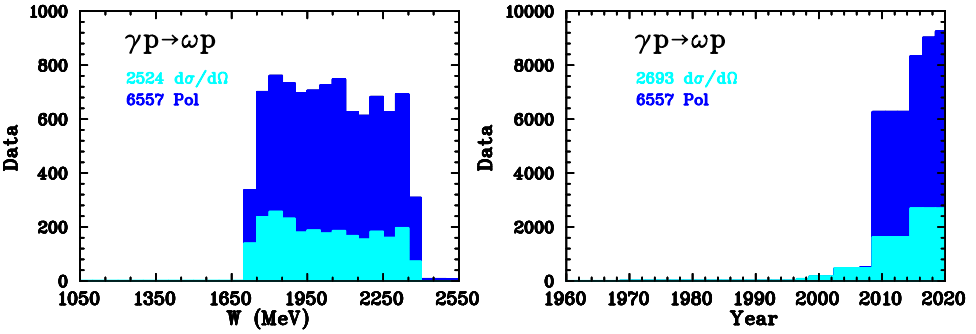

Fig. 16. Database for $\gamma p \to \omega p$. The notation is the same as in Fig. 6.

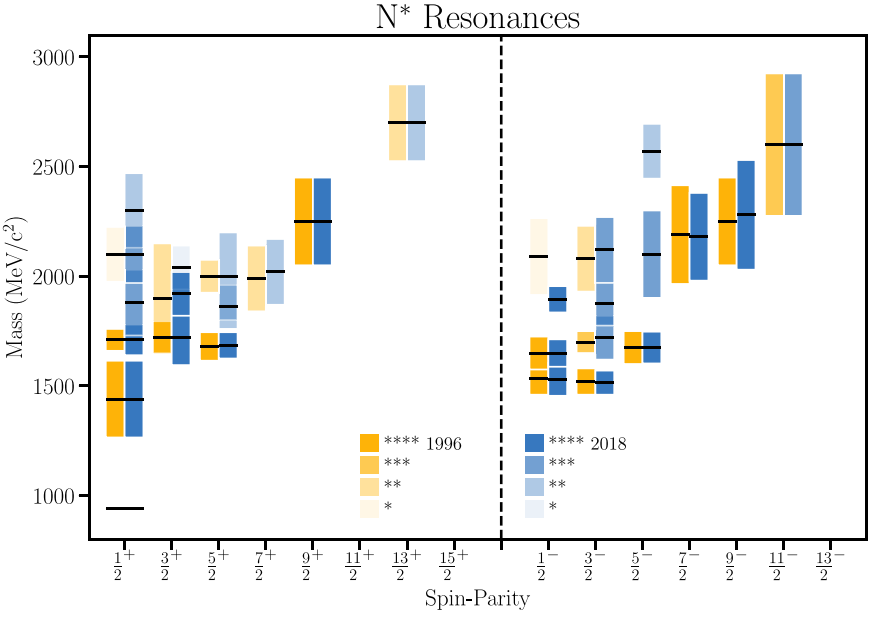

Fig. 17. Comparison of the N^* spectrum from the PDG of 1996 with 2018 editions.

two pion photoproduction was performed with DAPHNE at MAMI [180]. This experiment extracted total cross sections for three double pion channels: $\sigma_{tot}(p\pi^+\pi^-)$, $\sigma_{tot}(n\pi^+\pi^0)$, and $\sigma_{tot}(p\pi^0\pi^0)$. The measurements were done for photon energies from 400 to 800 MeV. SAPHIR extended the photon energy range for $\pi^+\pi^-$ up to 2.6 GeV. In this experiment they were able to extract differential cross sections and use Dalitz-plot analysis to isolate different contributions [181]. The first polarization measurements for this reaction were done by CLAS [182]. That experiment used circularly polarized photon beam and extracted the helicity asymmetry I^c for photon energies from 1.35 to 2.30 GeV. The latest measurements of this channel were done by CLAS [183]. This experiment covered the range of the center of mass energies from 1.6 to 2.0 GeV. High statistics allowed for the first time the extraction of nine 1-fold differential cross section and the determination of photocouplings of some known resonances.

For the $\pi^0\pi^0$ channel a series of experiments were performed at MAMI-B with TAPS on a proton target [184,185] and a deuteron target [186] from threshold to 820 MeV photon energies. The measurements were continued with the Crystal Ball/TAPS [187] combination. The addition of the Crystal Ball allowed the access of the $\pi^0\pi^+$ channel as well. With the extended energy reach of MAMI-C, the measurement with the Crystal Ball/TAPS on the proton and neutron was performed up to 1.4 GeV [188–192]. GRAAL extended measurements up to 1.5 GeV photon energy and in addition to the cross section they also took advantage of the linearly polarized photon beam and extracted Σ, the beam asymmetry, for this reaction [193]. Meanwhile the CBELSA collaboration did not stand idle, but joined the effort [194–197], further extending the energy reach up to 2.5 GeV. They also contributed polarization measurements of I^s and I^c [197].

The natural next step after $\pi^0\pi^0$ from the experimental point of view was to study $\pi^0\eta$, which has a similar topology. The first measurement of this reaction channel was reported by GRAAL. As usual for the GRAAL photon energy range up to 1.5 GeV, they presented total and differential cross section together with beam asymmetry Σ [198]. This was followed up

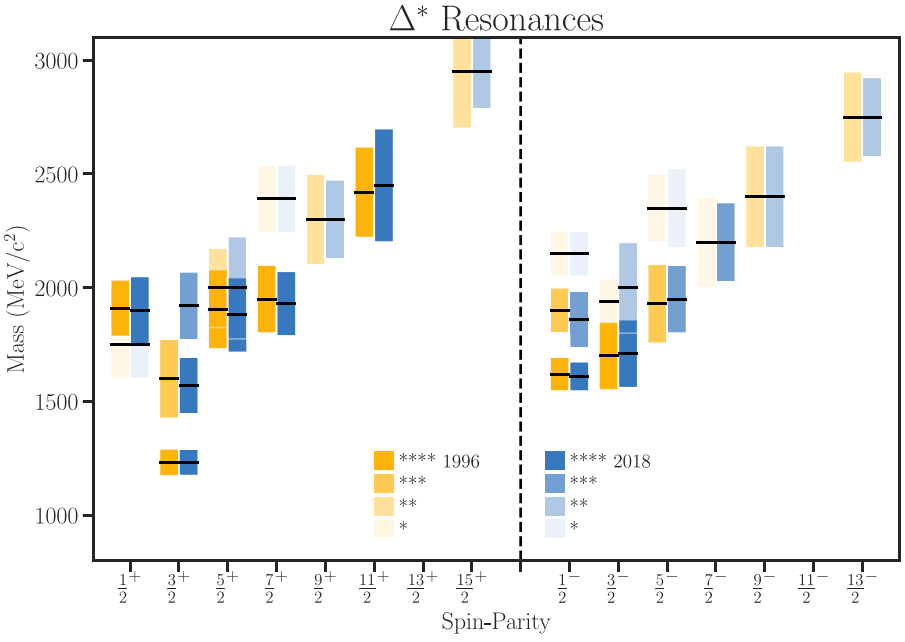

Fig. 18. Comparison of the Δ^* spectrum from the PDG of 1996 with 2018 editions.

Table 19
Comparison of N^* summary tables from PDG for the years 1996 and 2018. "–" means the cell is not present for that year.

Particle	J^P	Year	Overall status	Status as seen in									
				$N\gamma$	$N\pi$	$\Delta\pi$	$N\sigma$	$N\eta$	ΛK	ΣK	$N\rho$	$N\omega$	$N\eta'$
N	$1/2^+$	1996	****										
		2018	****										
$N(1440)$	$1/2^+$	1996	****	***	***	***	–	*			*	–	–
		2018	****	****	****	****							
$N(1520)$	$3/2^-$	1996	****	****	****	****	–	*			****	–	–
		2018	****	****	****	****	**	****					
$N(1535)$	$1/2^-$	1996	****	***	****	*	–	****			**	–	–
		2018	****	****	****	***	*	****					
$N(1650)$	$1/2^-$	1996	****	***	****	***	–	*	***	**	**	–	–
		2018	****	****	****	***	*	****	*				
$N(1675)$	$5/2^-$	1996	****	***	****	****	–	*	*		*	–	–
		2018	****	****	****	****	***	****	*	*			
$N(1680)$	$5/2^+$	1996	****	****	****	****	–				****	–	–
		2018	****	****	****	****	***	****	*	*			
$N(1700)$	$3/2^-$	1996	***	**	***	**	–	*	**	*	*	–	–
		2018	***	**	***	***	*	*			*		
$N(1710)$	$1/2^+$	1996	***	***	***	**	–	**	**	*	*	–	–
		2018	****	****	****	*		***	**	*	*	*	
$N(1720)$	$3/2^+$	1996	****	**	****	*	–	*	**	*	**	–	–
		2018	****	****	****	***	*	*	****	*	*	*	
$N(1860)$	$5/2^+$	1996	–	–	–	–	–	–	–	–	–	–	–
		2018	**	*	**		*	*					
$N(1875)$	$3/2^-$	1996	–	–	–	–	–	–	–	–	–	–	–
		2018	***	**	**	*	**	*	*	*	*	*	
$N(1880)$	$1/2^+$	1996	–	–	–	–	–	–	–	–	–	–	–
		2018	***	**	*	**	**	*	**	**		**	
$N(1895)$	$1/2^-$	1996	–	–	–	–	–	–	–	–	–	–	–
		2018	****	****	*	*	*	****	**	**	*	**	****

(*continued on next page*)

Table 19 (*continued*).

Particle	J^P	Year	Overall status	Status as seen in									
				$N\gamma$	$N\pi$	$\Delta\pi$	$N\sigma$	$N\eta$	ΛK	ΣK	$N\rho$	$N\omega$	$N\eta'$
$N(1900)$	$3/2^+$	1996	**		**		–				**	–	–
		2018	****	****	**	**	*	*	**	**		*	**
$N(1900)$	$7/2^+$	1996	**	*	**		–	*	*	*		–	–
		2018	**	**	**			*	*	*			
$N(2000)$	$5/2^+$	1996	**		**	*	–	*	*	*	**	–	–
		2018	**	**	*	**	*	*				*	
$N(2040)$	$3/2^+$	1996	–	–	–	–	–	–	–	–	–	–	–
		2018	*	*									
$N(2060)$	$5/2^+$	1996	–	–	–	–	–	–	–	–	–	–	–
		2018	***	***	**	*	*	*	*	*	*	*	
$N(2080)$	$3/2^-$	1996	**	*	**		–	*	*			–	–
		2018	–	–	–	–	–	–	–	–	–	–	–
$N(2090)$	$1/2^-$	1996	*		*		–					–	–
		2018	–	–	–	–	–	–	–	–	–	–	–
$N(2100)$	$1/2^+$	1996	**		**	*	–	*	*	*	**	–	–
		2018	**	**	*	**	*	*				*	
$N(2120)$	$3/2^-$	1996	–	–	–	–	–	–	–	–	–	–	–
		2018	***	***	**	**	**		**	*		*	*
$N(2190)$	$7/2^-$	1996	****	*	****		–	*	*	*	**	–	–
		2018	****	****	****	****	**	*	**	*	*	*	
$N(2200)$	$5/2^-$	1996	**		**		–	*	*			–	–
		2018	–	–	–	–	–	–	–	–	–	–	–
$N(2220)$	$9/2^+$	1996	****		****		–	*				–	–
		2018	****	**	****			*	*	*			
$N(2250)$	$9/2^-$	1996	****		****		–	*				–	–
		2018	****	**	****			*	*	*			
$N(2300)$	$1/2^+$	1996	–	–	–	–	–	–	–	–	–	–	–
		2018	**		**								
$N(2570)$	$5/2^-$	1996	–	–	–	–	–	–	–	–	–	–	–
		2018	**		**								
$N(2600)$	$11/2^-$	1996	***		***		–					–	–
		2018	***		***		–					–	–
$N(2700)$	$13/2^+$	1996	**		**		–					–	–
		2018	**		**		–					–	–

****	Existence is certain
***	Existence is very likely
**	Evidence of existence is fair
*	Evidence of existence is poor

by CBELSA in a series of measurements covering photon energies up to 2.5 GeV [199–202]. This experiment produced total and differential cross sections together with polarization observables Σ, I^s and I^c. Crystal Ball/TAPS at MAMI-C measured total and differential cross sections and beam asymmetries [203–208], which was followed by beam–target polarization measurements [209].

6. What have we learned from these data so far

In the previous sections of this review, we have presented all the experimental photoproduction data obtained in the last two decades. We conclude by summarizing how this plethora of data has expanded our knowledge of nucleon excited states. Tables 19 and 20 compare the non-strange baryon summary tables from the PDG for the 1996 [210] and 2018 [34] editions. Figs. 17 and 18 complement the tables by showing the spectra of states graphically, where masses and widths are represented by solid lines and boxes, respectively, and the star rating is represented by the shading. The first thing one notices while looking at these tables and figures is that *none* of the listed states has been left untouched, with one exception alone: the nucleon ground state. The tables show only the "star status" of the resonances. Quite often the knowledge of the resonance parameters improves while "star status" remains unchanged. The latest edition of PDG lists nine new states. Three states which have not received confirmation have been removed. The most of the changes are in N^* table, and not so much in the table of Δ^*'s. Most new information on nucleon resonances over the last two decades has come from photoproduction experiments, while in the past it was mostly from πN scattering.

Table 20
Comparison of Δ^* summary tables from PDG for the years 1996 and 2018. "–" means the cell is not present for that year.

Particle	J^P	Year	Overall status	Status as seen in					
				$N\gamma$	$N\pi$	$\Delta\pi$	ΣK	$N\rho$	$\Delta\eta$
$\Delta(1232)$	$3/2^+$	1996	****	****	****				–
		2018	****	****	****				
$\Delta(1600)$	$3/2^+$	1996	***	**	***	***		*	–
		2018	****	****	***	****			
$\Delta(1620)$	$1/2^-$	1996	****	***	****	****		****	–
		2018	****	****	****	****			
$\Delta(1700)$	$3/2^-$	1996	****	***	****	***	*	**	–
		2018	****	****	****	****	*	*	
$\Delta(1750)$	$1/2^+$	1996	*		*				–
		2018	*	*	*		*		
$\Delta(1900)$	$1/2^-$	1996	***	*	***	*	*	**	–
		2018	***	***	***	*	**	*	
$\Delta(1905)$	$5/2^+$	1996	****	***	****	**	*	**	–
		2018	****	****	****	**	*	*	**
$\Delta(1910)$	$1/2^+$	1996	****	*	****	*	*	*	–
		2018	****	***	****	**	**		*
$\Delta(1920)$	$3/2^+$	1996	***	*	***	**	*		–
		2018	***	***	***	***	**		**
$\Delta(1930)$	$5/2^-$	1996	***	**	***		*		–
		2018	***	***	***	*	*		
$\Delta(1940)$	$3/2^-$	1996	*		*				–
		2018	**	*	**	*			*
$\Delta(1950)$	$7/2^+$	1996	****	****	****	****	*	*	–
		2018	**	****	****	**	***		
$\Delta(2000)$	$5/2^+$	1996	**					**	–
		2018	**	*	**	*		*	
$\Delta(2150)$	$1/2^-$	1996	*		*				–
		2018	*		*				
$\Delta(2200)$	$7/2^-$	1996	*		*				–
		2018	***	***	**	***	**		
$\Delta(2300)$	$9/2^+$	1996	**		**				–
		2018	**		**				
$\Delta(2350)$	$5/2^-$	1996	*		*				–
		2018	*		*				
$\Delta(2390)$	$7/2^+$	1996	*		*				–
		2018	*		*				
$\Delta(2400)$	$9/2^-$	1996	**		**				–
		2018	**	**	**				
$\Delta(2420)$	$11/2^+$	1996	****		****				–
		2018	****	*	****				
$\Delta(2750)$	$13/2^-$	1996	**		**				–
		2018	**		**				
$\Delta(2950)$	$15/2^+$	1996	**		**				–
		2018	**		**				

****	Existence is certain
***	Existence is very likely
**	Evidence of existence is fair
*	Evidence of existence is poor

Nature gives us an additional powerful tool: an isospin filter. Photoproduction of the final states with isospin $I = 0$ mesons (η, η', ω), or $I = 0$ baryons, Λ's, cannot be directly coupled to Δ's. As can be seen from Table 19, most of the changes come exactly for these final states. New columns for $N\omega$ and $N\eta'$ have been added. Couplings to these states were not known previously. Double meson production established couplings of several resonances to the σN decay channel, which again was not known previously. Double meson production data also allowed the identification of sequential decays and established couplings of some of the higher mass Δ^*-resonances to $\Delta\eta$, which were not known before.

Please cite this article as: D.G. Ireland, E. Pasyuk and I. Strakovsky, Photoproduction reactions and non-strange baryon spectroscopy, Progress in Particle and Nuclear Physics (2019) 103752, https://doi.org/10.1016/j.ppnp.2019.103752.

These advances did not occur easily. It took time and effort for the information in the newly accumulated data sets to be translated into new knowledge of the baryon spectrum. As we described earlier, the renaissance of photoproduction started around mid 1990s. The first major overhaul of the non-strange baryon table happened in 2012 [211]. This represented the point at which the amount of new data needed to make an impact reached a critical mass. One remarkable example is new evidence for the $\Delta(2200)7/2^-$. This was a poorly known "1-star" state with only visible couplings to $N\pi$. New high accuracy polarization data from pion photoproduction were then added to the database. A coupled channel analysis revealed this resonance coupling to many channels: π^+n, π^0p, $K\Sigma$, $\pi^0\pi^0p$, $\pi^0\eta p$ [212]. In the latest edition of PDG, its status was upgraded to "3-star". This example also demonstrates the strength of applying a coupled channel approach to the data.

To conclude, it would be no exaggeration to say that non-strange baryon spectroscopy is quite healthy today. Several "missing" resonances have been found. New photoproduction data keep coming and there are no signs of a decline any time soon.

Acknowledgments

The work of D.I. was supported by the United Kingdom's Science and Technology Facilities Council (STFC) from grant number ST/P004458/1. The work of I.S. was supported in part by the US Department of Energy Grant DE–SC0016583. This material in part is based upon work supported by the U.S. Department of Energy, Office of Science, USA, Office of Nuclear Physics, USA under contract No. DE–AC05–06OR23177. We thank V. L. Kashevarov and V. Sokhoyan for their valuable suggestions.

Notice: Authored by Jefferson Science Associates, LLC under U.S. DOE Contract No. DE–AC05–06OR23177. The U.S. Government retains a non-exclusive, paid-up, irrevocable, world-wide license to publish or reproduce this manuscript for U.S. Government purposes.

References

[1] C.M.G. Lattes, et al., Nature 159 (1947) 694.
[2] E.M. McMillan, J.M. Peterson, R.S. White, Science 110 (1949) 579.
[3] J. Steinberger, W.K.H. Panofsky, J. Steller, Phys. Rev. 78 (1950) 802.
[4] A. Silverman, M. Stearns, Phys. Rev. 83 (1951) 853.
[5] W.K.H. Panofsky, J. Steinberger, J. Steller, Phys. Rev. 86 (1952) 180.
[6] A. Silverman, M. Stearnst, Phys. Rev. 88 (1952) 1225.
[7] G. Cocconi, A. Silverman, Phys. Rev. 88 (1952) 1230.
[8] J. Steinberger, A.S. Bishop, Phys. Rev. 78 (1950) 493.
[9] J. Steinberger, A.S. Bishop, Phys. Rev. 78 (1950) 494.
[10] A.S. Bishop, J. Steinberger, L.J. Coom, Phys. Rev. 80 (1950) 291.
[11] J. Steinberger, A.S. Bishop, Phys. Rev. 86 (1952) 171.
[12] R.S. White, M.J. Jacobson, A.G. Schulz, Phys. Rev. 88 (1952) 836.
[13] H.L. Anderson, E. Fermi, E.A. Long, D.E. Nagle, Phys. Rev. 85 (1952) 936.
[14] A.J.G. Hey, R.L. Kelly, Phys. Rep. 96 (1983) 71.
[15] W.J. Briscoe, M. Doering, H. Haberzettl, I.I. Strakovsky, R.L. Workman, GWU CNS DAC SAID database, 2019, http://gwdac.phys.gwu.edu/analysis/pr-analysis.html.
[16] V. Crede, W. Roberts, Rep. Progr. Phys. 76 (2013) 07631.
[17] B. Krusche, Progr. Part. Nucl. Phys. 67 (2012) 412.
[18] B. Krusche, Eur. Phys. J. Spec. Top. 198 (2011) 199.
[19] E. Klempt, J.-M. Richard, Rev. Modern Phys. 82 (2010) 1095.
[20] B. Krusche, S. Schadmand, Progr. Part. Nucl. Phys. 51 (2003) 399.
[21] I.S. Barker, A. Donnachie, J.K. Storrow, Nuclear Phys. B 95 (1975) 347.
[22] C.G. Fasano, F. Tabakin, B. Saghai, Phys. Rev. C 46 (6) (1992) 2430–2455.
[23] W.-T. Chiang, F. Tabakin, Phys. Rev. C 55 (1997) 2054.
[24] D. Ireland, Phys. Rev. C 82 (2) (2010) 025204.
[25] G.F. Chew, M.L. Goldberger, F.E. Low, Y. Nambu, Phys. Rev. 106 (6) (1957) 1345–1355.
[26] M. Jacob, G.C. Wick, Ann. Physics 7 (4) (1959) 404–428.
[27] A.M. Sandorfi, S. Hoblit, H. Kamano, T.-S.H. Lee, J. Phys. G 38 (2011) 053001.
[28] W. Roberts, T. Oed, Phys. Rev. C 71 (2005) 055201.
[29] K. Schilling, P. Seyboth, G. Wolf, Nuclear Phys. B 15 (2) (1970) 397–412.
[30] W.M. Kloet, W.-T. Chiang, F. Tabakin, Phys. Rev. C 58 (2) (1998) 1086–1097.
[31] J. Hadamard, Sur les Problemes aux Derivees Partielles et leur Signification Physique, Princeton Univ. Bulletin., 1902, p. 49.
[32] A.N. Tikhonov, V.Y. Arsenin, Solutions of Ill-Posed Problems, Winston, New York, 1977.
[33] R.A. Arndt, W.J. Briscoe, M.W. Paris, I.I. Strakovsky, R.L. Workman, Chin. Phys. C 33 (2009) 1063.
[34] M. Tanabashi, et al., (Particle Data Group), Phys. Rev. D 98 (2018) 030001.
[35] K.M. Watson, Phys. Rev. 88 (1952) 1163.
[36] R.L. Walker, Phys. Rev. 182 (1969) 1729.
[37] A.B. Migdal, JETP 1 (1955) 2.
[38] V.E. Tarasov, W.J. Briscoe, H. Gao, A.E. Kudryavtsev, I.I. Strakovsky, Phys. Rev. C 84 (2011) 035203.
[39] V.E. Tarasov, A.E. Kudryavtsev, W.J. Briscoe, B. Krusche, I.I. Strakovsky, M. Ostrick, Phys. At. Nucl. 79 (2016) 216.
[40] R.A. Arndt, W.J. Briscoe, I.I. Strakovsky, R.L. Workman, Phys. Rev. C 74 (2006) 045205.
[41] R.A. Arndt, W.J. Briscoe, I.I. Strakovsky, R.L. Workman, Phys. Rev. C 76 (2007) 025209.
[42] M. Dugger, et al., (CLAS Collaboration), Phys. Rev. C 76 (2007) 025211.
[43] R. Machleidt, Phys. Rev. C 63 (2001) 024001.

[44] W. Chen, et al., Phys. Rev. C 86 (2012) 015206.
[45] P. Mattione, et al., (CLAS Collaboration), Phys. Rev. C 96 (2017) 035204.
[46] D. Ho, et al., (CLAS Collaboration), Phys. Rev. Lett. 118 (2017) 242002.
[47] M. Dieterle, et al., (A2 Collaboration at MAMI), Phys. Lett. B 770 (2017) 523.
[48] B.A. Mecking, et al., (CLAS Collaboration), Nucl. Instrum. Methods A 503 (2003) 513.
[49] D.I. Sober, et al., Nucl. Instrum. Methods A 440 (2000) 263.
[50] C.D. Keith, et al., Nucl. Instrum. Methods A 684 (2012) 27.
[51] M.M. Lowry, et al., Nucl. Instrum. Methods A 815 (2016) 31.
[52] O. Bartalini, et al., (GRAAL Collaboration), Eur. Phys. J. A 26 (2005) 399.
[53] H. Schmieden, Few-Body Syst. 59 (2018) 135.
[54] I. Anthony, et al., Nucl. Instrum. Methods A 301 (1991) 230.
[55] A. Reiter, et al., Eur. Phys. J. A 30 (2006) 461.
[56] J.C. McGeorge, et al., Eur. Phys. J. A 37 (2008) 129.
[57] G. Audit, et al., Nucl. Instrum. Methods A 301 (1991) 473.
[58] A.R. Gabler, et al., Nucl. Instrum. Methods A 346 (1994) 168.
[59] J.R.M. Annand, et al., (A2 Collaboration at MAMI), Phys. Rev. C 93 (2016) 055209.
[60] E.D. Bloom, C.W. Peck, Annu. Rev. Nucl. Sci. 33 (1983) 143.
[61] W. Hillert, Eur. Phys. J. A 28 (s1) (2006) 139.
[62] W.J. Schwille, et al., Nucl. Instrum. Methods A 344 (1994) 470.
[63] E. Aker, et al., (Crystal Barrel Collaboration), Nucl. Instrum. Methods A 321 (1992) 69.
[64] A. Thiel, et al., (CBELSA/TAPS Collaboration), Eur. Phys. J. A 53 (2017) 8.
[65] T. Nakano, et al., Nuclear Phys. A 684 (2001) 71c.
[66] N. Muramatsu, et al., Nucl. Instrum. Methods A 737 (2014) 184.
[67] M. Niiyama, et al., in: Proceedings of the 14th International Conference on Meson-Nucleon Physics and the Structure of the Nucleon (MENU2016), 2017, p. 020009.
[68] Y. Matsumura, et al., in: Proceedings of the 10th International Workshop on the Physics of Excited Nucleons (NSTAR2015), 2016, p. 032011.
[69] F. Hinode, et al., W.B. Liu, et al., (Eds.), in: Proceedings Ofthe Second Asian Particle Accelerator Conference, 2001, p. 106.
[70] H. Yamazaki, et al., Nucl. Instrum. Methods A 536 (2005) 70.
[71] M. Kaneta, et al., (NKS2 Collaboration), Nuclear Phys. A 914 (2013) 69.
[72] K. Suziki, et al., Modern Phys. Lett. A 24 (2009) 978.
[73] HEPdata database, 2019, https://www.hepdata.net.
[74] CLAS physiscs database, 2019, https://clasweb.jlab.org/physicsdb/.
[75] A. Schmidt, et al., (A2 Collaboration at MAMI), Phys. Rev. Lett. 87 (2001) 232501.
[76] D. Hornidge, et al., (A2 and CB-TAPS Collaborations), Phys. Rev. Lett. 111 (2013) 062004.
[77] R. Beck, Eur. Phys. J. A 28 S01 (2006) 173.
[78] G. Blanpied, et al., (LEGS Collaboration), Phys. Rev. C 64 (2001) 025203.
[79] P. Adlarson, et al., (A2 Collaboration at MAMI), Phys. Rev. C 92 (2015) 024617.
[80] J. Ahrens, et al., (GDH and A2 Collaborations), Eur. Phys. J. A 21 (2004) 323.
[81] O. Bartholomy, et al., (CBELSA Collaboration), Phys. Rev. Lett. 94 (2005) 012003.
[82] S. Schumann, et al., (Crystal Ball at MAMI, TAPS and A2 Collaborations), Eur. Phys. J. A 43 (2010) 269.
[83] O. Bartalini, et al., (GRAAL Collaboration), Eur. Phys. J. A 26 (2005) 399.
[84] P. Ahrens, et al., (GDH and A2 Collaborations), Phys. Rev. Lett. 88 (2002) 232002.
[85] B. Krusche, et al., Eur. Phys. J. A 6 (1999) 309.
[86] M. Kunkel, et al., (CLAS Collaboration), Phys. Rev. C 98 (2018) 015207.
[87] M. Sumihama, et al., (LEPS Collaboration), Phys. Lett. B 657 (2007) 32.
[88] S. Gardner, et al., (A2 Collaboration at MAMI), Eur. Phys. J. A 52 (2016) 333.
[89] F.V. Adamian, et al., Phys. Rev. C 63 (2001) 054606.
[90] D. Elsner, et al., (CBELSA/TAPS Collaboration), Eur. Phys. J. A 39 (2009) 373.
[91] N. Sparks, et al., (CBELSA/TAPS Collaboration), Phys. Rev. C 81 (2010) 065210.
[92] M. Dugger, et al., (CLAS Collaboration), Phys. Rev. C 88 (2013) 065203.
[93] J. Hartmann, et al., (CBELSA/TAPS Collaboration), Phys. Lett. B 748 (2015) 212.
[94] K. Wijesooriya, et al., (Jefferson Lab Hall A Collaboration), Phys. Rev. C 66 (2002) 034614.
[95] W. Luo, et al., (GEp-III and GEp2γ Collaborations), Phys. Rev. Lett. 108 (2012) 222004.
[96] S. Schumann, et al., (A2 Collaboration at MAMI), Phys. Lett. B 750 (2015) 252.
[97] A. Bock, et al., (PHOENICS Collaboration), Phys. Rev. Lett. 81 (1998) 534.
[98] J. Ahrens, et al., (GDH and A2 Collaborations), Eur. Phys. J. A 26 (2005) 135.
[99] A. Thiel, et al., (CBELSA/TAPS Collaboration), Phys. Rev. Lett. 109 (2012) 102001.
[100] J.R.M. Annand, et al., (A2 Collaboration at MAMI), Phys. Rev. C 93 (2016) 055209.
[101] M. Gottschall, et al., (CBELSA/TAPS Collaboration), Phys. Rev. Lett. 112 (2014) 012003.
[102] M.H. Sikora, et al., (A2 Collaboration at MAMI), Phys. Rev. Lett. 112 (2014) 022501.
[103] E. Korkmaz, et al., Phys. Rev. Lett. 83 (1999) 3609.
[104] D. Branford, et al., Phys. Rev. C 61 (2000) 014603.
[105] R. Beck, et al., Phys. Rev. C 61 (2000) 034604.
[106] H.W. Dannhausen, et al., Eur. Phys. J. A 11 (2001) 441.
[107] J. Ahrens, et al., (GDH and A2 Collaborations), Phys. Rev. C 74 (2006) 054204.
[108] M. Dugger, et al., (CLAS Collaboration), Phys. Rev. C 79 (2009) 065206.
[109] L.Y. Zhu, et al., (Jefferson Lab Hall A and Jefferson Lab E94-104 Collaborations), Phys. Rev. C 71 (2005) 044603.
[110] H. Kohri, et al., (LEPS Collaboration), Phys. Rev. C 97 (2018) 015205.
[111] J. Ajaka, et al., (GRAAL Collaboration), Phys. Lett. B 475 (2000) 372.
[112] O. Bartalini, et al., (GRAAL Collaboration), Phys. Lett. B 544 (2002) 113.
[113] S. Strauch, et al., (CLAS Collaboration), Phys. Lett. B 750 (2015) 53.
[114] A. Shafi, et al., (Crystal Ball Collaboration), Phys. Rev. C 70 (2004) 035204.
[115] W.J. Briscoe, A.E. Kudryavtsev, P. Pedroni, I.I. Strakovsky, V.E. Tarasov, R.L. Workman, Phys. Rev. C 86 (2012) 065207.
[116] W. Chen, et al., (CLAS Collaboration), Phys. Rev. Lett. 103 (2009) 012301.

Please cite this article as: D.G. Ireland, E. Pasyuk and I. Strakovsky, Photoproduction reactions and non-strange baryon spectroscopy, Progress in Particle and Nuclear Physics (2019) 103752, https://doi.org/10.1016/j.ppnp.2019.103752.

[117] W. Chen, H. Gao, W.J. Briscoe, D. Dutta, A.E. Kudryavtsev, M. Mirazita, M.W. Paris, P. Ross, S. Stepanyan, I.I. Strakovsky, V.E. Tarasov, R.L. Workman, Phys. Rev. C 86 (2012) 015206.
[118] G. Mandaglio, et al., (GRAAL Collaboration), Phys. Rev. C 82 (2010) 045209.
[119] R.D. Salvo, et al., (GRAAL Collaboration), Eur. Phys. J. A 42 (2009) 151.
[120] E.F. McNicoll, et al., (A2 Collaboration at MAMI), Phys. Rev. C 82 (2010) 035208.
[121] V.L. Kashevarov, et al., (A2 Collaboration at MAMI), Phys. Rev. Lett. 118 (2017) 212001.
[122] O. Bartalini, et al., (GRAAL Collaboration), Eur. Phys. J. A 33 (2007) 169.
[123] T. Nakabayashi, et al., Phys. Rev. C 74 (2006) 035202.
[124] M. Dugger, et al., (CLAS Collaboration), Phys. Rev. Lett. 89 (2002) 222002.
[125] M. Williams, et al., (CLAS Collaboration), Phys. Rev. C 80 (2009) 045213.
[126] V. Crede, et al., (CBELSA Collaboration), Phys. Rev. Lett. 94 (2005) 012004.
[127] J. Ahrens, et al., (GDH and A2 Collaboration), Eur. Phys. J. A 17 (2003) 241.
[128] V. Crede, et al., (CBELSA/TAPS Collaboration), Phys. Rev. C 80 (2009) 055202.
[129] M. Sumihama, et al., (LEPS Collaboration), Phys. Rev. C 80 (2009) 052201.
[130] D. Elsner, et al., (CBELSA/TAPS Collaboration), Eur. Phys. J. A 33 (2007) 147.
[131] P. Collins, et al., (CLAS Collaboration), Phys. Lett. B 771 (2017) 213.
[132] C.S. Akondi, et al., (A2 Collaboration at MAMI), Phys. Rev. Lett. 113 (2014) 102001.
[133] I. Senderovich, et al., (CLAS Collaboration), Phys. Lett. B 755 (2016) 64.
[134] I. Jaegle, et al., (CBELSA/TAPS Collaboration), Phys. Rev. Lett. 100 (2008) 252002.
[135] L. Witthauer, et al., (CBELSA/TAPS Collaboration), Eur. Phys. J. A 53 (2017) 58.
[136] D. Werthmüller, et al., (A2 Collaboration at MAMI), Phys. Rev. Lett. 111 (2013) 232001.
[137] A. Fantini, et al., (GRAAL Collaboration), Phys. Rev. C 78 (2008) 015203.
[138] L. Witthauer, et al., (A2 Collaboration at MAMI), Phys. Rev. Lett. 117 (2016) 132502.
[139] R. Plötzke, et al., (SAPHIR Collaboration), Phys. Lett. B 444 (1998) 555.
[140] M. Dugger, et al., (CLAS Collaboration), Phys. Rev. Lett. 96 (2006) 062001.
[141] P.L. Sandri, et al., (GRAAL Collaboration), Eur. Phys. J. A 51 (2015) 77.
[142] S. Capstick, W. Roberts, Phys. Rev. D 58 (7) (1998) 074011.
[143] M.Q. Tran, et al., (SAPHIR Collaboration), Phys. Lett. B 445 (1998) 20.
[144] K.H. Glander, et al., (SAPHIR Collaboration), Eur. Phys. J. A 19 (2004) 251.
[145] M. Sumihama, et al., (LEPS Collaboration), Phys. Rev. C 73 (2006) 035214.
[146] R.G.T. Zegers, et al., (LEPS Collaboration), Phys. Rev. Lett. 91 (2003) 092001.
[147] K. Hicks, et al., (LEPS Collaboration), Phys. Rev. C 76 (2007) 042201(R).
[148] A. Lleres, et al., (GRAAL Collaboration), Eur. Phys. J. A 31 (2007) 79.
[149] A. Lleres, et al., (GRAAL Collaboration), Eur. Phys. J. A 39 (2009) 149.
[150] J.W.C. McNabb, et al., (CLAS Collaboration), Phys. Rev. C 69 (2004) 042201(R).
[151] R.K. Bradford, et al., (CLAS Collaboration), Phys. Rev. C 75 (2007) 035205.
[152] M.E. McCracken, et al., (CLAS Collaboration), Phys. Rev. C 81 (2010) 025201.
[153] B. Dey, et al., (CLAS Collaboration), Phys. Rev. C 82 (2010) 025202.
[154] C.A. Patterson, et al., (CLAS Collaboration), Phys. Rev. C 93 (2016) 065201.
[155] T.C. Jude, et al., (A2 Collaboration at MAMI), Phys. Lett. B 735 (2014) 112.
[156] R.K. Bradford, et al., (CLAS Collaboration), Phys. Rev. C 73 (2006) 035202.
[157] M. Ablikim, et al., Nat. Phys. (2019) 1.
[158] D.G. Ireland, M. Döring, D.I. Glazier, J. Haidenbauer, M. Mai, R. Murray-Smith, D. Rönchen, arXiv:1904.07616, 2019.
[159] R. Lawall, et al., (SAPHIR Collaboration), Eur. Phys. J. A 24 (2005) 275.
[160] H. Kohri, et al., (LEPS Collaboration), Phys. Rev. Lett. 97 (2006) 082003.
[161] P. Aguar-Bartolome, et al., (A2 Collaboration at MAMI), Phys. Rev. C 88 (2013) 044601.
[162] S. Görs, et al., (SAPHIR Collaboration), Phys. Lett. B 464 (1999) 331.
[163] S.A. Pereira, et al., (CLAS Collaboration), Phys. Lett. B 688 (2010) 289.
[164] N. Compton, et al., (CLAS Collaboration), Phys. Rev. C 96 (2017) 065201.
[165] D.H. Ho, et al., (CLAS Collaboration), Phys. Rev. C 98 (2018) 045205.
[166] I. Strakovsky, et al., (A2 Collaboration at MAMI), Phys. Rev. C 91 (2015) 045207.
[167] J. Barth, et al., (SAPHIR Collaboration), Eur. Phys. J. A 18 (2003) 117.
[168] M. Williams, et al., (CLAS Collaboration), Phys. Rev. C 80 (2009) 065208.
[169] F. Dietz, et al., (CBELSA/TAPS Collaboration), Eur. Phys. J. A 51 (2015) 6.
[170] A. Wilson, et al., (CBELSA/TAPS Collaboration), Phys. Lett. B 749 (2015) 407.
[171] F. Klein, et al., (CBELSA/TAPS Collaboration), Phys. Rev. D 78 (2008) 117101.
[172] P. Roy, et al., (CLAS Collaboration), Phys. Rev. C 97 (2018) 055202.
[173] P. Collins, et al., (CLAS Collaboration), Phys. Lett. B 773 (2017) 112.
[174] J. Ajaka, et al., (GRAAL Collaboration), Phys. Rev. Lett. 96 (2006) 132003.
[175] P. Roy, et al., (CLAS Collaboration), Phys. Rev. Lett. 122 (2019) 162001.
[176] H. Eberhardt, et al., (CBELSA/TAPS Collaboration), Phys. Lett. B 750 (2015) 453.
[177] Z. Akbar, et al., (CLAS Collaboration), Phys. Rev. C 96 (2017) 065209.
[178] R. Erbe, et al., (ABBHHM Collaboration), Phys. Rev. 188 (1969) 2060.
[179] G. Gialanella, et al., Nuovo Cimento A 63 (1969) 892.
[180] A. Braghieria, et al., Phys. Lett. B 363 (1995) 46.
[181] C. Wu, et al., Eur. Phys. J. A 23 (2005) 317.
[182] S. Strauch, et al., (CLAS Collaboration), Phys. Rev. Lett. 95 (2005) 162003.
[183] E. Golovach, et al., (CLAS Collaboration), Phys. Lett. B 788 (2019) 371.
[184] F. Härter, et al., Phys. Lett. B 401 (1997) 229.
[185] M. Wolf, et al., Eur. Phys. J. A 9 (2000) 5.
[186] V. Kleber, et al., Eur. Phys. J. A 9 (2000) 1.
[187] F. Zehr, et al., (The Crystal Ball at MAMI, TAPS, and A2 Collaborations), Eur. Phys. J. A 48 (2012) 98.
[188] V.L. Kashevarov, et al., (A2 Collaboration), Phys. Rev. C 85 (2012) 064610.
[189] M. Dieterle, et al., (A2 Collaboration), Eur. Phys. J. A 51 (2015) 142.
[190] D. Krambrich, et al., (Crystal Ball at MAMI, TAPS, and A2 Collaborations), Phys. Rev. Lett. 103 (2009) 052002.

Please cite this article as: D.G. Ireland, E. Pasyuk and I. Strakovsky, Photoproduction reactions and non-strange baryon spectroscopy, Progress in Particle and Nuclear Physics (2019) 103752, https://doi.org/10.1016/j.ppnp.2019.103752.

[191] M. Oberle, et al., Phys. Lett. B 721 (2013) 237.
[192] M. Oberle, et al., (Crystal Ball at MAMI, TAPS and A2 Collaborations), Eur. Phys. J. A 50 (2014) 54.
[193] Y. Assafiri, et al., (GRAAL Collaboration), Phys. Rev. Lett. 90 (2003) 222001.
[194] U. Thoma, et al., (CB-ELSA Collaboration), Phys. Lett. B 659 (2008) 87.
[195] A.V. Sarantsev, et al., (CB-ELSA and A2-TAPS Collaborations), Phys. Lett. B 659 (2008) 94.
[196] A. Thiel, et al., Phys. Rev. Lett. 114 (2015) 091803.
[197] V. Sokhoyan, et al., (CBELSA/TAPS Collaboration), Eur. Phys. J. A 51 (2015) 95, Erratum: ibid. 187.
[198] J. Ajaka, et al., (GRAAL Collaboration), Phys. Rev. Lett. 100 (2008) 052003.
[199] I. Horn, et al., (CB-ELSA Collaboration), Phys. Rev. Lett. 101 (2008) 202002.
[200] I. Horn, et al., (CB-ELSA Collaboration), Eur. Phys. J. A 38 (2008) 173.
[201] E. Gutz, et al., (CBELSA/TAPS Collaboration), Phys. Lett. B 687 (2010) 11.
[202] E. Gutz, et al., (CBELSA/TAPS Collaboration), Eur. Phys. J. A 50 (2014) 74.
[203] V.L. Kashevarov, et al., (Crystal Ball at MAMI, TAPS and A2 Collaborations), Eur. Phys. J. A 42 (2009) 141.
[204] V.L. Kashevarov, et al., (Crystal Ball at MAMI, TAPS and A2 Collaborations), Phys. Lett. B 693 (2010) 551.
[205] A. Käser, et al., Phys. Lett. B 748 (2015) 244.
[206] A. Käser, et al., (A2 collaboration), Eur. Phys. J. A 52 (2016) 272.
[207] A. Käser, et al., Phys. Lett. B 786 (2018) 305.
[208] V. Sokhoyan, et al., (A2 Collaboration at MAMI), Phys. Rev. C 97 (2018) 055212.
[209] J.R.M. Annanad, et al., (A2 Collaboration), Phys. Rev. C 91 (2015) 055208.
[210] R. Barnett, et al., (Particle Data Group), Phys. Rev. D 54 (1996) 1.
[211] J. Beringer, et al., (Particle Data Group), Phys. Rev. D 86 (2012) 010001.
[212] V. Anisovich, et al., Phys. Lett. B 766 (2017) 357.

Please cite this article as: D.G. Ireland, E. Pasyuk and I. Strakovsky, Photoproduction reactions and non-strange baryon spectroscopy, Progress in Particle and Nuclear Physics (2019) 103752, https://doi.org/10.1016/j.ppnp.2019.103752.